Unified Two-Time-Scale Modeling and Hybrid ZVS Modulation of *LCC–LCC* Compensated IPT System With Wide Input Voltage Range

Kai He, *Student Member, IEEE*, Fei Gao, *Member, IEEE*, Xin Liu, *Member, IEEE*, Ying Jiang, Xijun Yang, *Member, IEEE*, and Daniel J. Rogers, *Senior Member, IEEE*

***Abstract*—The operating frequencies of the dc–dc converter connected to the distributed energy resources and inductive power transfer (IPT) systems are often different, which makes it difficult to model the cascaded system accurately by using a single time scale. In this article, a two-time-scale model (TTSM) consisting of fast-time-scale and slow-time-scale state variables, which has high accuracy and efficient calculation, is proposed for the cascaded four-switch buck–boost IPT (FSBB-IPT) system. The full-mode operation and zero-voltage-switching (ZVS) conditions of the cascaded system are studied based on the TTSM. To overcome the failure of the traditional ZVS modulation strategies of the first-stage converter in the FSBB-IPT system, a hybrid ZVS modulation scheme in the new time scale is developed to reduce the root-mean-square value of the inductor current and improve the efficiency. An FSBB-IPT prototype with a wide input voltage range is built to verify the effectiveness of the proposed modulation scheme.**

***Index Terms*—Four-switch buck–boost (FSBB), hybrid modulation, inductive power transfer (IPT), two-time-scale model (TTSM), zero voltage switching (ZVS).**

I. Introduction

DISTRIBUTED energy resources (DERs) such as photovoltaics and battery energy storage systems play a critical role in reducing carbon emissions and improving the resilience of future smart grids [1]. Utilization convenience and wide distribution are remarkable characteristics of the DERs. Besides, once the distributed systems lose the support from the main grids and become isolated, DERs can ensure the power supply continuity [2]. Inductive power transfer (IPT) system has been applied in diverse scenarios, such as electric vehicles [3], autonomous underwater vehicles [3], [5], biomedical implant equipment [6], [7], uncrewed aerial vehicles [8], and consumer electronics [9], among others.

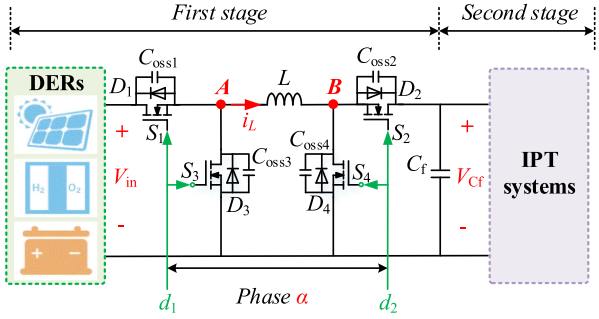

Fig. 1. Typical structure of the cascaded system under study.

However, limited by the battery capacity, the endurance time and cruising range are still too short for the applications, which is one of the bottlenecks in the further development of IPT systems. As shown in Fig. 1, a four-switch buck–boost (FSBB) converter, which is used as an interface converter for DERs to power IPT systems, has the voltage step-up and voltage step-down ability and low voltage stress of power switches. Compared with the conventional buck and boost converters, there exists three degrees of control freedom in the FSBB converter, i.e., the duty cycles d_1 and d_2 of the two switching legs and the phase-shift angle α between the two duty cycles. In addition, different from the buck–boost converter, the output voltage polarity is the same as the input.

Therefore, it is an advantageous candidate for the microgrids with various dc DERs [10], [11], [12]. When IPT systems are directly powered by the DERs, the problems can be effectively addressed. In Fig. 1, the first stage contains the DERs, FSBB converter, and the bus capacitor C_f. The second stage is the IPT system. S_1–S_4 are power switches, and D_1–D_4 and C_{oss1}–C_{oss4} are the antiparallel body diodes and the output capacitances of the MOSFETs, respectively. L is the inductor between the two legs. V_{in} is the output voltage of the DERs. V_{Cf} is the output voltage of the FSBB converter.

Received 25 July 2024; revised 18 October 2024 and 2 December 2024; accepted 29 December 2024. Date of publication 8 January 2025; date of current version 27 August 2025. This work was supported in part by the National Natural Science Foundation of China under Grant 52377194 and Grant 52307012 and in part by the Shanghai Jiao Tong University Deep Blue Program under Grant SL2022MS009. Recommended for publication by Associate Editor J. Acero. *(Corresponding author: Fei Gao.)*

Kai He, Fei Gao, and Xijun Yang are with the State Key Laboratory of Submarine Geoscience, Shanghai Jiao Tong University, Shanghai 200240, China, and also with the Key Laboratory of Control of Power Transmission and Conversion, Ministry of Education, School of Electrical Engineering, Shanghai Jiao Tong University, Shanghai 200240, China (e-mail: hk_3823@sjtu.edu.cn; fei.gao@sjtu.edu.cn; yangxijun@sjtu.edu.cn).

Xin Liu is with the Shenzhen Institute for Advanced Study, University of Electronic Science and Technology of China, Shenzhen 518110, China (e-mail: liu_xin@uestc.edu.cn).

Ying Jiang is with the Shanghai Dianji University, Shanghai 201306, China (e-mail: jiangy@sdju.edu.cn).

Daniel J. Rogers is with the University of Oxford, OX1 2JD Oxford, U.K. (e-mail: dan.rogers@eng.ox.ac.uk).

Color versions of one or more figures in this article are available at https://doi.org/10.1109/TPEL.2025.3527508.

Digital Object Identifier 10.1109/TPEL.2025.3527508

TABLE I
EXISTING MODELING METHODS FOR THE CASCADED SYSTEMS

Literature	[13]-[15]	[16]	[17]-[19]	[20]	**This article**
Modeling method	DTM	SSM	IBM	SSAM	TTSM
Cascaded topology	Buck-buck/boost-boost	Buck-buck	Buck-buck/LCL-LCL	Buck-buck	FSBB-IPT system
Operating frequencies	$f_M = f_N$	/	$f_M = f_N$ / $f_M \neq f_N$	$f_M \neq f_N$	$f_M \neq f_N$
Time scale	Single	Single	Single	Single	Two

Because of the two-stage structure, the characteristics of the cascaded system are quite different from the single-stage converter [13]. Specifically, the ripple interaction of the two stages cannot be ignored for accurate modeling and may cause the instability of the whole system. The operating frequencies of the two stages are often different, which means that the system depends simultaneously on a "fast" and "slow" time. In other words, when the two stages are not completely decoupled by the bus capacitor C_f, there will exist variables in two-time scales.

To investigate the characteristics of cascaded systems, as presented in Table I, numerous works focus on the accurate modeling, including discrete-time models (DTMs) [13], [14], [15], [16] and continuous-time models [17], [18], [19], [20]. For a uniform expression, the operating frequencies of the first stage and second stage are defined as f_M and f_N, respectively. Although the effect of the load converter on the source buck converter is analyzed in [13] by establishing the discrete-time mapping model, it fails to account for scenarios where the operating frequencies of the two stages are different. A small-step discretization method is developed to study the two-stage cascaded peak current-mode controlled boost converter in [14]; however, it only accomplishes the discretization of the system's operating states within a single switching period, without extending to map in the full-mode period. Furthermore, it does not achieve mode rearrangement under a unified discrete-time step. Similarly, the problem of modeling the cascaded system with different frequencies is simplified to modeling the system with the same operating frequency in [15], while only the normalization of duty cycles is addressed. The small-signal model (SSM) is established in [16] for n-stage cascaded dc–dc converters but it does not take into account multiple time scales and only models the local behavior of the system. In [17], [18], and [19], the stability and dynamic performance of the cascaded dc–dc systems are studied by using impedance-based models (IBMs). The open-loop characteristics of the cascaded buck–buck converter in dc microgrid are analyzed based on the state-space averaging model (SSAM) [20].

The aforementioned models either only consider cascaded systems with the single-time-scale variables, or fail to achieve discrete-time mapping under a unified time scale, or do not address the mode rearrangement over the full-mode operating period. When the cascaded systems are nonfully decoupled and variables in two-time scales occur, the existing models either become not applicable or suffer from low accuracy.

The ZVS modulation in wide input and output voltage ranges is another important issue for the optimal operation of the studied system [21], [22], [23], [24], [25], [26]. A ZVS control scheme based on discontinuous conduction mode is proposed in [21] to achieve full-range ZVS for all switches and low-current-switching turn-OFF for part of switches. To overcome the sensitivity to switching noise and avoid the requirement for lookup tables (LUTs), a closed-form solution for ZVS modulation and minimum root-mean-square (RMS) inductor current of the FSBB converters are studied in [22]. The dead time between the two switches of one bridge is considered for ZVS analysis of the integrated bidirectional dc–dc converter in [23]. Pulsewidth modulation with phase-shift control (PSC) [24], constant frequency, and multifrequency pseudocontinuous conduction mode ZVS modulation [10], and three-mode variable-frequency ZVS modulation [25] are also studied for the high-efficiency operation of the first-stage FSBB converter.

However, the abovementioned modulation schemes mainly concentrate on minimizing the RMS value of the inductor current, and only the single-stage operation of the cascaded system is considered. The full-mode operation and synchronous ZVS modulation of the two stages in the cascaded FSBB-IPT system are not studied.

In this article, a two-time-scale model (TTSM) is proposed for the cascaded FSBB-IPT system, which consists of fast-time-scale and slow-time-scale variables. The explicit TTSM helps in obtaining the ZVS conditions for both the FSBB converter and *LCC–LCC* compensated IPT system. A hybrid ZVS modulation strategy, which is conducted on the new time scale and can minimize the RMS value of the inductor current in the full-mode operation, is also analyzed.

The main contributions of this article are as follows.

1) Aiming at the multi-time-scale variables resulting from incomplete decoupling in the cascaded FSBB-IPT system, and considering the bus voltage ripple, a TTSM is proposed, which has high accuracy.
2) Through time-scale transformation, full-mode rearrangement, and discrete-time mapping, the proposed method achieves mapping under a unified time scale T_m in the full-mode operating period T_{max_com}, effectively resolving the challenge of handling multiple-time-scale variables by one unified model.
3) A hybrid ZVS modulation method based on the new time scale T_m is proposed. Both stages of the cascaded system adopt the same sampling frequency f_m, which can significantly reduce the computational burden of the modulation strategy and facilitate the electromagnetic interference (EMI) filter design.
4) With the help of the inherent phase shift β between the two stages, the synchronous ZVS modulation of the front-end FSBB converter and rear-end inverter is achieved, thereby eliminating the need for synchronization communication in the cascaded system.

The rest of the article is organized as follows. Section II gives the introduction of the FSBB-IPT system with the full-mode operation and analyzes the boundary conditions. The TTSM of the cascaded system is developed in Section III. Section IV analyzes the hybrid ZVS modulation scheme. Section V

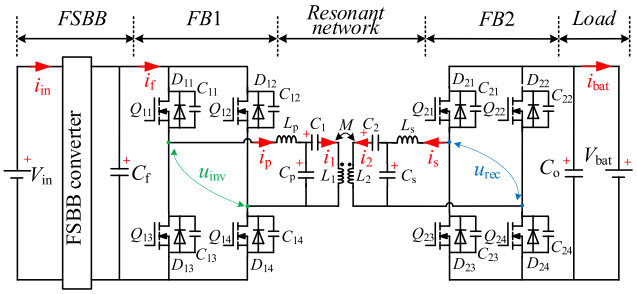

Fig. 2. Schematic of the cascaded FSBB-IPT system.

illustrates the experimental results and comparison. Finally, Section VI concludes the article.

II. Full-Mode Operation of the FSBB-IPT System

A. Basic Principles

The FSBB converter is shown in Fig. 1. S_1 and S_3, S_2 and S_4 are switched ON/OFF complementarily. d_1 and d_2 are the duty cycles of S_1 and S_2, respectively. α is the phase-shift angle. The voltage gain σ of the converter can be derived as [24]

$$V_{\mathrm{Cf}} = d_1 V_{\mathrm{in}}/d_2 = \sigma V_{\mathrm{in}}. \tag{1}$$

Fig. 2 shows the schematic of the cascaded FSBB-IPT system. The *LCC–LCC* compensated IPT system is defined as the second stage of the cascaded system. FB1 and FB2 represent the active bridges on the primary and secondary sides. Q_{11}–Q_{14} and Q_{21}–Q_{24} are the power switches (MOSFETs) of FB1 and FB2, respectively. D_{11}–D_{14} and C_{11}–C_{14}, D_{21}–D_{24} and C_{21}–C_{24} are the antiparallel diodes and output capacitances of the MOSFETs. L_1 and L_2 are the coil inductances of the transmitting and receiving coils. M is the mutual inductance between the two coils and expressed as $k(L_1L_2)^{1/2}$, where k is the coupling coefficient. L_{p}, C_{p}, C_1 and L_{s}, C_{s}, C_2 are the compensation inductors and capacitors, respectively. V_{bat} is the voltage of the battery packs.

The parameters of the compensation network are designed as

$$\begin{cases} \omega_{\mathrm{N}} L_{\mathrm{p}} = 1/\omega_{\mathrm{N}} C_{\mathrm{p}} = \omega_{\mathrm{N}} L_1 - 1/\omega_{\mathrm{N}} C_1 \\ \omega_{\mathrm{N}} L_{\mathrm{s}} = 1/\omega_{\mathrm{N}} C_{\mathrm{s}} = \omega_{\mathrm{N}} L_2 - 1/\omega_{\mathrm{N}} C_2 \end{cases} \tag{2}$$

where $\omega_{\mathrm{N}} = 2\pi f_{\mathrm{N}}$ and f_{N} is the resonant frequency of the second-stage IPT system.

B. Full-Mode Operation

The operating modes of the cascaded system consist of multiple switching states in sequence during one common period $T_{\mathrm{max\_com}}$, which is named "full-mode operation" in this article.

Fig. 3 shows the general operating waveforms with the hybrid ZVS modulation strategy when the FSBB converter operates in boost mode ($\sigma > 1$). When $\sigma < 1$ and $\sigma = 1$, it is defined as buck mode and equal mode, respectively. More operating modes of the FSBB converter have been analyzed in [12]. The operating periods of the first and second stages are defined as T_{M} and T_{N}, and $T_{\mathrm{M}} = \varepsilon T_{\mathrm{N}}$ (ε is positive, and $\varepsilon > 1$ in this article). The dead time of all switches of the system is noted as t_{d}.

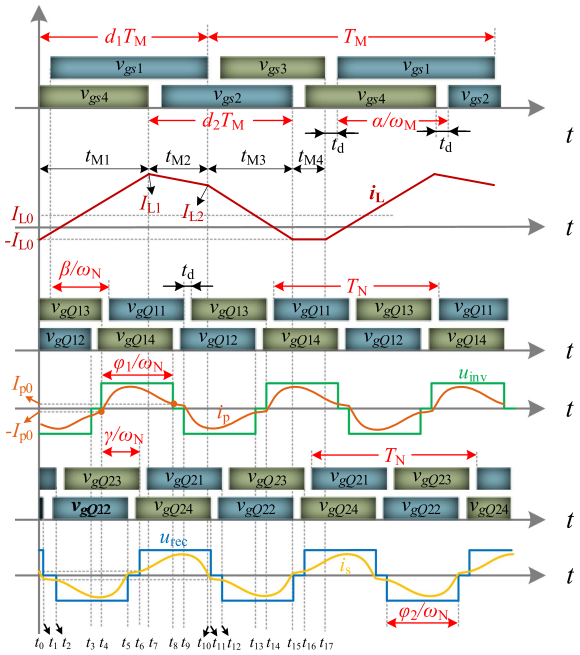

Fig. 3. Key waveforms of the cascaded system when $\sigma > 1$ and $f_{\mathrm{M}} < f_{\mathrm{N}}$ ($0 \le \beta/\omega_{\mathrm{N}} \le d_1 T_{\mathrm{M}}$).

TABLE II
Possible Operating Modes With Hybrid Modulation

Mode	$T_{\mathrm{M}} > T_{\mathrm{N}}$	$T_{\mathrm{M}} < T_{\mathrm{N}}$
I	$0 \le \beta/\omega_{\mathrm{N}} \le \alpha/\omega_{\mathrm{M}}$	$0 \le \beta/\omega_{\mathrm{N}} \le \alpha/\omega_{\mathrm{M}}$
II	$0 \le \beta/\omega_{\mathrm{N}} \le d_1 T_{\mathrm{M}}$	$0 \le \beta/\omega_{\mathrm{N}} \le d_1 T_{\mathrm{M}}$
III	$0 \le \beta/\omega_{\mathrm{N}} \le \alpha/\omega_{\mathrm{M}} + d_2 T_{\mathrm{M}}$	$0 \le \beta/\omega_{\mathrm{N}} \le \alpha/\omega_{\mathrm{M}} + d_2 T_{\mathrm{M}}$
IV	$0 \le \beta/\omega_{\mathrm{N}} \le T_{\mathrm{M}}$	$0 \le \beta/\omega_{\mathrm{N}} \le T_{\mathrm{M}}$
V	/	$T_{\mathrm{M}} \le \beta/\omega_{\mathrm{N}} \le T_{\mathrm{M}} + \alpha/\omega_{\mathrm{M}}$
…	/	…

It can be seen from Fig. 3 that there exist two-time scales in the cascaded FSBB-IPT system due to the different operating frequencies, which leads to the slow-time-scale state variable, i.e., the inductor current i_{L} and the capacitor voltage u_{Cf}, and the fast-time-scale state variables, i.e., the output current i_{p} of FB1, the input current i_{s} of FB2, etc. What is more, a phase shift $\beta = \omega_{\mathrm{N}} t$ ($\beta \in (0, 2\pi)$) between the two stages, which is defined in the fast-time scale, occurs. It is the inherent characteristic of the multiple-time-scale cascaded systems. Thus, different from the single-stage system, there is one more degree of freedom when studying ZVS modulation.

One of the full-mode operations of the FSBB-IPT system when $0 < \beta/\omega_{\mathrm{N}} \le d_1 T_{\mathrm{M}}$ is presented in Fig. 3. More possible operating modes of the cascaded system with hybrid ZVS modulation are given in Table II.

The second stage employs a PSC strategy. The outer phase shift between FB1 and FB2 is noted as γ. To simplify the analysis, only the switching states of S_1, S_2, Q_{11}, Q_{12}, Q_{21}, and Q_{22} are considered to present the full-mode operation of the system. "P" and "N" indicate switching ON and OFF, respectively. There are $2^6 = 64$ possible switching sequences in the full-mode operation, which are PNNPPN, PNNPPP, …, NNPNPN. When

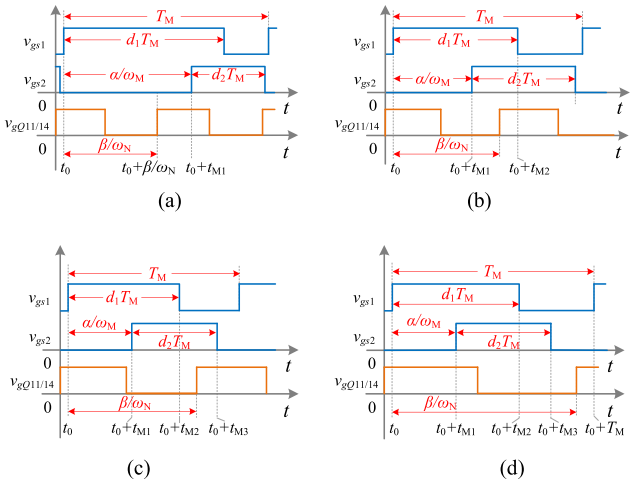

Fig. 4. Possible phase shifts $\beta = \omega_N t$ when $f_M < f_N$. (a) $0 < \beta/\omega_N \le \alpha/\omega_M$. (b) $0 < \beta/\omega_N \le d_1 T_M$. (c) $0 < \beta/\omega_N \le \alpha/\omega_M + d_2 T_M$. (d) $0 < \beta/\omega_N \le T_M$.

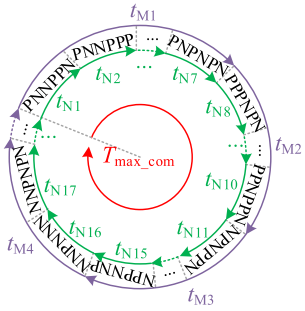

Fig. 5. Full-mode operation of the FSBB-IPT system.

$T_M > T_N$ and the dead time is ignored, the possible phase shifts $\beta = \omega_N t$ with the hybrid modulation are shown in Fig. 4. Fig. 5 presents the switching process of the FSBB-IPT system with the full-mode operation shown in Fig. 3, where the outer purple circle and the inner green circle represent the operating states of the first stage and second stage, respectively. T_{max_com} is the full-mode operating period, and the arrows indicate the trend of state changes. The principle of time marking is the same as that in Fig. 3, which means that for every change in the switching sequence, the time label is added by one. Notably, there could be multiple switching states in sequence in one operating mode presented in Table II when the ratio ε changes, only one operating state of each mode during the period T_M is given in Fig. 5. When the resonant frequency of the second stage is fixed, the number of the switching sequences increases with the operating frequency of the first stage.

Without loss of the generality, the mode II when $T_M > T_N$ is taken as an example to further explain the full-mode operation of the cascaded system, which is presented in Fig. 3. The time intervals t_{Mi} ($i = 1, 2, 3, 4$) of the first stage and t_{Ni} ($t_{Ni} = t_i - t_{i-1}$, $i = 1, 2, \ldots, 17$) of the second stage meet

$$\sum_{i=1}^{4} t_{Mi} = T_M, \sum_{i=5}^{14} t_{Ni} = \sum_{i=6}^{16} t_{Ni} = T_N \tag{3}$$

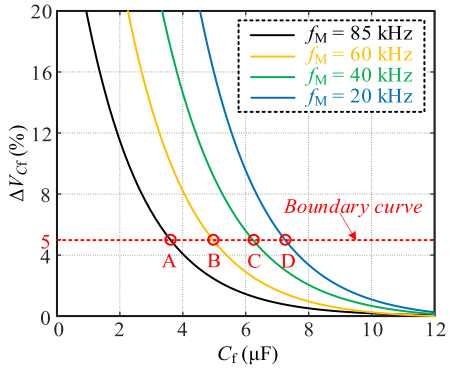

Fig. 6. Relationship between ΔV_{Cf} and C_f studied in this article when $V_{in} = 400$ V, $\sigma = 1$, and $f_N = 85$ kHz.

$$\sum_{i=1}^{7} t_{Ni} = t_{M1}, \sum_{i=8}^{10} t_{Ni} = t_{M2}, \sum_{i=11}^{15} t_{Ni} = t_{M3}, \sum_{i=16}^{17} t_{Ni} = t_{M4}. \tag{4}$$

Besides, it can be seen from Fig. 5 that during one full-mode operating period T_{max_com}, the switching sequences of the two stages are not synchronous but independent, which is because of two-time scales existing in the cascaded system.

C. Boundary Conditions

The power decoupling capacitor C_f serves as a bridge in the two-stage FSBB-IPT system. Since the operating frequency f_M of the front-end FSBB converter is variable, there are two coupling scenarios. 1) The operating frequencies f_M and f_N are the same, and the capacitor voltage ripple rate ΔV_{Cf} exceeds 5% in the full-power range. 2) Different operating frequencies f_M and f_N result in multiple-time-scale variables existing in the system despite the adoption of advanced control strategies. To determine the coupling boundary value C_{f_boun} of the bus capacitor, based on the analysis in [27] and [28], Fig. 6 provides the curves illustrating the relationship between the capacitor values and the bus voltage ripples, where the voltage ripple rate ΔV_{Cf} of bus capacitor is defined as

$$\Delta V_{Cf} = \frac{|u_{Cf\_max} - u_{Cf\_min}|}{V_{costant}} \times 100\% \tag{5}$$

where u_{Cf_max} and u_{Cf_min} are the maximum and minimum values of u_{Cf}, and $V_{costant}$ is the average value of u_{Cf}. To reduce the reactive power and ensure dc–dc efficiency, the second-stage IPT system typically operates at the resonant frequency. Therefore, Fig. 6 investigates the trend of the boundary decoupling capacitor when f_N is fixed at 85 kHz and f_M varies from 20 to 85 kHz. In Fig. 6, the red line represents the boundary between coupled and decoupled operation modes for the two-stage FSBB-IPT system. Above the red line, where ΔV_{Cf} exceeds 5%, the FSBB-IPT system is considered to be coupled; below the red line, it is considered to be decoupled. As illustrated in Table III, points A, B, C, and D correspond to the boundary capacitor values for different f_M. It can be observed from Fig. 6 and Table III that when $f_M = f_N = 85$ kHz, the capacitor voltage ripple will exceed

TABLE III
BOUNDARY CAPACITANCES UNDER DIFFERENT f_M

Points	A	B	C	D
C_{f_boun} (μF)	3.60	4.94	6.24	7.26

5% when the capacitance of C_f is smaller than 3.60 μF. When f_M = 60/40/20 kHz, the boundary capacitances C_{f_boun} of C_f are 4.94 μF, 6.24 μF, and 7.26 μF, respectively. Besides, the voltage ripple of the bus capacitor is roughly inversely related to the capacitance of C_f, and the boundary capacitance C_{f_boun} increases as the operating frequency f_M decreases.

III. TWO-TIME-SCALE MODELING

A. Definition of the Two-Time Scales

In the cascaded FSBB-IPT system, more than two-time scales can be used to characterize the system behaviors accurately, and the simplest case is analyzed in this article.

Define t as the "fast" time and $\tau = \varepsilon t$ as the "slow" time, the systems of the form

$$\begin{aligned} \dot{\boldsymbol{x}}_M &= \varepsilon f\left(t, \varepsilon t, \boldsymbol{x}_M, \boldsymbol{x}_N, \varepsilon\right) \\ \dot{\boldsymbol{x}}_N &= g\left(t, \varepsilon t, \boldsymbol{x}_M, \boldsymbol{x}_N, \varepsilon\right) \end{aligned} \tag{6}$$

are considered, where $\boldsymbol{x}_M = [i_L\ u_{Cf}]^T$ and $\boldsymbol{x}_N = [i_p\ u_{Cp}\ u_{C1}\ i_1\ i_2\ u_{C2}\ u_{Cs}\ i_s]^T$ are the state vectors in slow time scale and fast time scale, respectively, and are the differentials of $\boldsymbol{x}_M$ and $\boldsymbol{x}_N$. f and g are the system functions. Dots denote differentiation with respect to t.

The two-time scales t and $\tau = \varepsilon t$ are considered as two independent variables. Specifically, τ will be regarded as a constant on the fast time t. The coefficient ε is obtained as

$$\varepsilon = T_M/T_N = f_N/f_M. \tag{7}$$

For unified expression of the whole system, the state-space equation of the FSBB-IPT system can be expressed as

$$\begin{pmatrix} \dot{\boldsymbol{x}}_{M|\varepsilon t} \\ \varepsilon \dot{\boldsymbol{x}}_{N|t} \end{pmatrix} = \begin{pmatrix} \boldsymbol{M}_{11|\varepsilon t} & \boldsymbol{M}_{12|t} \\ \boldsymbol{M}_{21|\varepsilon t} & \boldsymbol{M}_{22|t} \end{pmatrix} \begin{pmatrix} \boldsymbol{x}_{M|\varepsilon t} \\ \boldsymbol{x}_{N|_t} \end{pmatrix} + \boldsymbol{N}_i \boldsymbol{U} \boldsymbol{G}_i \tag{8}$$

where $\boldsymbol{M} = [\boldsymbol{M}_{11}\ \boldsymbol{M}_{12}; \boldsymbol{M}_{21}\ \boldsymbol{M}_{22}]$ and $\boldsymbol{U} = \text{diag}\ \{V_{in}, V_{bat}\}$. $\boldsymbol{N}_i$ (i = 1, 2, …) are the system matrix and input matrix in the two independent time scales. $\boldsymbol{G}_i = [G_{i1}\ G_{i2}]^T$ (G_{i1} = 1/-1/0, G_{i2} = 1/-1) is the state vector that is defined according to the full-mode operation.

B. Derivation of the Proposed Model

The full-mode operation of the FSBB-IPT system operating in mode II is taken as an example to present the derivation of the TTSM. The dead time of the power switches and the equivalent series resistances of the passive components are not considered to simplify the analysis.

1) Step 1: Time-Scale Transformation: As shown in (6) and (8), the state variables $\boldsymbol{x}_{M|\tau}$ and $\boldsymbol{x}_{N|t}$ are periodic in $\tau = \varepsilon t$ and t, respectively. The purpose of time-scale transformation is to transfer the cascaded system into a singularly perturbed system, which is presented in Fig. 7. Because the relationship between T_M and T_N is clearly defined in (7), the functions f and g in (6) can be considered to depend only on a new common time scale T_m = min_com$\{T_M, T_N\}$, which is defined as

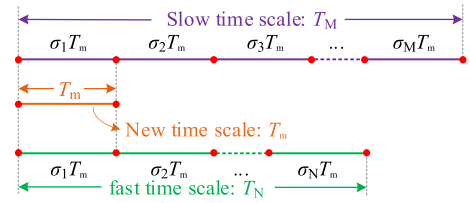

Fig. 7. Schematic diagram of the time-scale transformation when $f_M < f_N$.

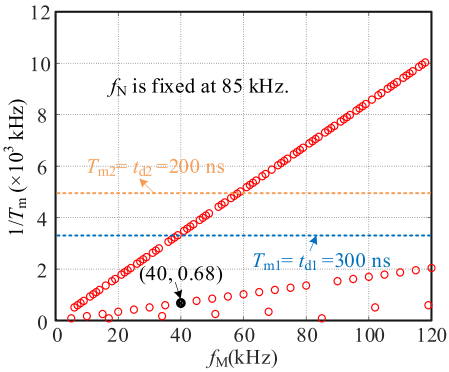

Fig. 8. Mapping points of $f_m = 1/T_m$ when f_N is fixed at 85 kHz.

$$T_m = T_M/\sigma_M = T_N/\sigma_N\ (\sigma_M/\sigma_N = \varepsilon) \tag{9}$$

$$\sum_{i=1}^{M} \sigma_i T_m = T_M, \sum_{i=1}^{N} \sigma_i T_m = T_N \tag{10}$$

where σ_M, $\sigma_N \in \boldsymbol{N}_+$. It should be noted that T_m is a new time scale for describing the system behavior, not the operating period of the system. In this article, $f_M = 1/T_M$ = 40 kHz, $f_N = 1/T_N$ = 85 kHz, $f_m = 1/T_m$ = 680 kHz, and T_{max_com} = 5 kHz. After the time-scale transformation, one can obtain the singularly perturbed system

$$\begin{aligned} \sigma_M \dot{\boldsymbol{x}}_M &= \varepsilon f\left(T_m, \boldsymbol{x}_M, \boldsymbol{x}_N, \varepsilon, \sigma_M\right) \\ \sigma_N \dot{\boldsymbol{x}}_N &= g\left(T_m, \boldsymbol{x}_M, \boldsymbol{x}_N, \varepsilon, \sigma_N\right). \end{aligned} \tag{11}$$

In the new time scale T_m, (8) can be expressed as

$$\begin{pmatrix} \sigma_M \dot{\boldsymbol{x}}_{M|T_m} \\ \sigma_N \dot{\boldsymbol{x}}_{N|T_m} \end{pmatrix} = \begin{pmatrix} \boldsymbol{M}_{11|T_m} & \boldsymbol{M}_{12|T_m} \\ \boldsymbol{M}_{21|T_m} & \boldsymbol{M}_{22|T_m} \end{pmatrix} \begin{pmatrix} \boldsymbol{x}_{M|T_m} \\ \boldsymbol{x}_{N|T_m} \end{pmatrix} + \boldsymbol{N}_i \boldsymbol{U} \boldsymbol{G}_i. \tag{12}$$

To demonstrate the determination of the new time scale T_m, Fig. 8 shows the mapping values of $f_m = 1/T_m$ for different f_M when f_N is fixed at 85 kHz. For computational feasibility, the iteration step for f_M is set to 1 kHz. In theory, the new time scale $T_m = 1/f_m$ should be chosen as small as possible for higher

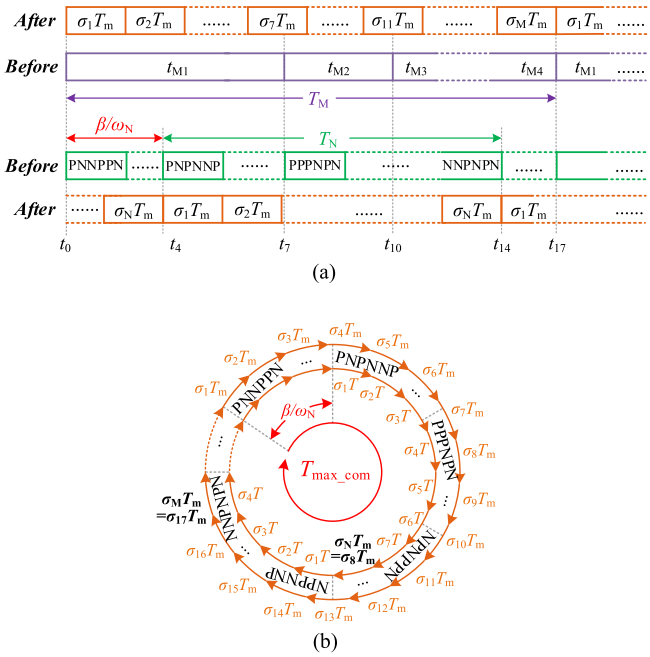

Fig. 9. Schematic diagram of the full-mode rearrangement when $\sigma > 1$ and $0 < \beta/\omega_N \le d_1 T_M$. (a) Basic principle. (b) Full-mode operation after rearrangement.

TABLE IV
TRANSFORMATION COEFFICIENTS ξ_{Mi_j}

Coefficient	Value	Coefficient	Value
ξ_{M1_1}~ξ_{M6_1}	$1/(\alpha\sigma_M)$	ξ_{M11_3}	$0.8/((\alpha+d_2-d_1)\sigma_M)$
ξ_{M7_1}	$0.8/(\alpha\sigma_M)$	ξ_{M12_3}~ξ_{M15_3}	$1/((\alpha+d_2-d_1)\sigma_M)$
ξ_{M7_2}	$0.2/((d_1-\alpha)\sigma_M)$	ξ_{M16_3}	$0.3/((\alpha+d_2-d_1)\sigma_M)$
ξ_{M8_2}~ξ_{M10_2}	$1/((d_1-\alpha)\sigma_M)$	ξ_{M16_4}	$0.7/((1-\alpha-d_2)\sigma_M)$
ξ_{M11_2}	$0.2/((d_1-\alpha)\sigma_M)$	ξ_{M17_4}	$1/((1-\alpha-d_2)\sigma_M)$

TABLE V
TRANSFORMATION COEFFICIENTS ξ_{Ni_j}

Coefficient	Values	Coefficient	Values
ξ_{N1_5}	$2\pi/(\sigma_N(\gamma-\pi+\varphi_2))$	ξ_{N5_10}	$2\pi/(\sigma_N(\gamma-\varphi_1))$
ξ_{N2_5}	$2\pi/(\sigma_N(\gamma-\pi+\varphi_2))$-$1/\sigma_N$	ξ_{N6_10}	1-$2\pi/(\sigma_N(\gamma-\varphi_1))$
ξ_{N2_6}/ξ_{N3_7}	1	ξ_{N6_11}/ξ_{N6_12}	1
ξ_{N3_8}	$(\pi-\varphi_2)/(\sigma_N\gamma)$	ξ_{N7_13}	$2\pi/(\sigma_N(\pi-\gamma))$
ξ_{N4_8}	$2\pi/(\sigma_N(\gamma+\varphi_1+\varphi_2)$-$(2\pi)/(\sigma_N^2))$	ξ_{N8_13}	$(2\pi-\sigma_N(\pi-\varphi_1))/(\sigma_N(\pi-\gamma))$
ξ_{N4_9}	1	ξ_{N8_14}	$2\pi/\sigma_N(\pi-\varphi_1)$

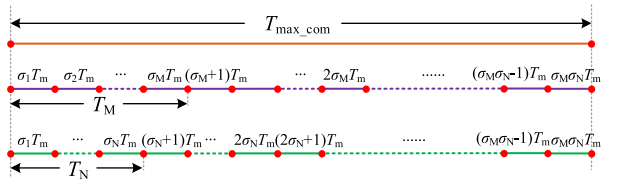

Fig. 10. Schematic diagram of the full-mode discrete-time mapping.

computational accuracy. However, to balance the effectiveness and speed of model calculations, the minimum value of T_m needs to be set to the dead time t_d. As shown in Fig. 8, when T_{m1} is greater than the dead time $t_{d1} = 300$ ns, at this point, $f_m \le 3.333 \times 10^3$ kHz, which corresponds to the area below the blue line and represents the valid selection range for the new time scale T_m. Conversely, above the black line where f_m is greater than 3.333×10^3 kHz, it indicates T_{m1} is smaller than t_{d1}, and thus should not be selected as the new scale. When the dead time changes to $t_{d2} = 200$ ns, the range of selection for the new time scale will accordingly increase.

2) Step 2: Full-Mode Rearrangement: The purpose of the full-mode rearrangement is to achieve matching between the full-mode operation and the new time scale T_m. The core idea of the mode rearrangement is that the switching sequences remain unchanged, and the slow time scale $\tau = \varepsilon t$ and the fast time scale t are scaled by using the coefficients ξ_{Mi_j} and ξ_{Ni_j}, respectively. Fig. 9 shows the comparison of the full-mode operation before and after rearrangement when taking mode II shown in Fig. 3 as an example. Specifically, $f_M = 40$ kHz, $f_N = 85$ kHz, $d_1 = 0.6$, $d_2 = 0.5$, and $\alpha = 0.4$. To simplify the analysis, the full-mode rearrangement is conducted for slow-time scale T_M and fast-time scale T_N by defining the trailing edges of v_{gs3} and v_{gQ13} as the reference time instants in the new time scale T_m, and the rearrangement coefficients are given in Tables IV and V.

ξ_{Mi_j} ($i = 1, 2, \ldots, \sigma_M$) and ξ_{Ni_j} ($i = 1, 2, \ldots, \sigma_N$) are the transformation coefficients of slow time scale and fast time scale, where subscript i represents the i_{th} new time scale T_m and subscript j represents the jth operating state analyzed in Section II-B. For example, ξ_{M2_3} is the rearrangement coefficient of the third operating state t_{M3} in the second new time scale $\sigma_2 T_m$. The full-mode operation of the system after rearrangement in the new time scale can be obtained as

$$\begin{cases} \xi_{M1\_1} t_{M1} = \sigma_1 T_m, \xi_{M2\_1} t_{M1} = \sigma_2 T_m, \ldots, \xi_{M6\_1} t_{M1} = \sigma_6 T_m \\ \xi_{M7\_1} t_{M1} + \xi_{M7\_2} t_{M2} = \sigma_7 T_m, \ldots, \xi_{M17\_1} t_{M4} = \sigma_{17} T_m, \ldots \end{cases} \tag{13}$$

$$\xi_{N1\_3} t_{N3} = \sigma_1 T_m, \xi_{N2\_3} t_{N3} = \sigma_2 T_m, \xi_{N3\_4} t_{N4} = \sigma_3 T_m, \ldots \tag{14}$$

where σ_i ($i = 1, 2, \ldots, \sigma_N, \ldots, \sigma_M$) should always be satisfied with (10).

It can be seen from Fig. 9 that $\sigma_M = 17$ and $\sigma_N = 8$ for the full-mode operation shown in Fig. 3. After the mode rearrangement, as shown in Fig. 9(b), the slow time scale and fast time scale will operate in the same time scale T_m, which means that the difficulty of describing the state variables in different time scales is solved.

3) Step 3: Full-Mode Discrete-Time Mapping: To ensure the accuracy of the proposed model, as shown in Fig. 10, the unified discrete-time mapping is conducted in the full-mode period T_{max_com} by using the new time scale T_m. Different from the DTMs analyzed in [14], the TTSM has uniform criteria for achieving discretization and all the full-mode operating states are considered during the mapping process.

The initial and final values of the period T_{max_com} are noted as $\boldsymbol{x}_{n|Tm}$ and $\boldsymbol{x}_{n+1|Tm}$, and ξ_{Mi_j}, ξ_{Ni_j} ($i = 1, 2, \ldots$) are the transformation coefficients obtained in *Step 2*. The discrete-time

mapping during one new time scale is given by

$$\begin{aligned}\boldsymbol{x}_{n(i)} &= \Gamma_{ni}\left(\boldsymbol{x}_{n(i-1)}, \xi_{\mathrm{M}i\_j}, \xi_{\mathrm{N}_{i\_j}}, T_{\mathrm{m}}\right) \\ &= e^{\boldsymbol{M}_i T_{n(i)}}\boldsymbol{x}_{n(i-1)} + \boldsymbol{\kappa}_{ni}\boldsymbol{U}\boldsymbol{G}_i \end{aligned} \tag{15}$$

where the index $i = 1, 2, \ldots, \sigma_{\mathrm{M}}\sigma_{\mathrm{N}}$ represents the new time scale T_{m} obtained in the full-mode rearrangement. In steady state, $\kappa_{\mathrm{n}(1)} = \kappa_{\mathrm{n}(\sigma \mathrm{M}\sigma \mathrm{N}+1)}$ and $\boldsymbol{x}_{\mathrm{n}(1)} = \boldsymbol{x}_{\mathrm{n}(\sigma \mathrm{M}\sigma \mathrm{N}+1)}$. Denoted $\boldsymbol{E}$ as the unit matrix, κ_{ni} can be expressed as

$$\begin{aligned}\boldsymbol{\kappa}_{ni}\left(\xi_{\mathrm{M}i\_j}, \xi_{\mathrm{N}_{i\_j}}, T_{\mathrm{m}}\right) &= \boldsymbol{\kappa}_{(n+1)_i}(\xi_{\mathrm{M}i\_j}, \xi_{\mathrm{N}_{i\_j}}, T_{\mathrm{m}}) \\ &= \int_{t_0}^{t_0+T_{ni}} e^{\boldsymbol{M}_i(T_{ni}-\rho)}d\rho. \end{aligned} \tag{16}$$

In (16), the integral calculation of κ_{ni} containing the tenth high-order exponential matrix cannot obtain accurate analytical solutions, thus, $\boldsymbol{\Phi} = e^{\boldsymbol{M}_i T_{\mathrm{m}}}$ needs to be further simplified as $\hat{\boldsymbol{\Phi}} = \boldsymbol{E} + T_{\mathrm{m}}\boldsymbol{M}_i\boldsymbol{\Psi}_n$. $\boldsymbol{\Psi}_n$ is given as [3]

$$\boldsymbol{\Psi}_n = \boldsymbol{E} + \frac{1}{2!}\boldsymbol{M}_i T_{\mathrm{m}} + \frac{1}{3!}(\boldsymbol{M}_i T_{\mathrm{m}})^2 + \cdots + \frac{1}{n!}(\boldsymbol{M}_{\mathrm{i}} T_{\mathrm{m}})^{n-1} \tag{17}$$

where n can be used to obtain arbitrary accuracy in numerical calculation.

The discrete-time mapping of the cascaded FSBB-IPT system with the full-mode operation is obtained as

$$\boldsymbol{x}_{n+1|T} = \hat{\boldsymbol{\Phi}}\left(\boldsymbol{\kappa}_{\mathrm{n}}\right)\boldsymbol{x}_{\mathrm{n}} + \boldsymbol{\Omega}\left(\boldsymbol{\kappa}_{\mathrm{n}}, \boldsymbol{U}\right) \tag{18}$$

where $\hat{\boldsymbol{\Phi}}(\boldsymbol{\kappa}_n) = e^{\boldsymbol{M}_i T_{\mathrm{max\_com}}}$ and

$$\boldsymbol{\Omega}(\boldsymbol{\kappa}_n, \boldsymbol{U}) = \sum_{i=1}^{\sigma_{\mathrm{M}}\sigma_{\mathrm{N}}} (e^{\boldsymbol{M}T_{\mathrm{max\_com}}} - \boldsymbol{E})e^{\boldsymbol{M}(T_{\mathrm{max\_com}} - \sum_1^i T_{n(i)})}\boldsymbol{\kappa}_{\mathrm{n}i}\boldsymbol{U}\boldsymbol{G}_i.$$

When the switching sequences are XPPNXX, XPNPXX, XPPPXX, and XPNNX, where "X" represents any switching state, κ_n can further be simplified as

$$\boldsymbol{\kappa}_{ni} = \boldsymbol{\kappa}_{(n+1)_i} = \boldsymbol{M}_i{}^{-1}\left(e^{\boldsymbol{M}_i T_{ni}} - \boldsymbol{E}\right)\boldsymbol{N}_i. \tag{19}$$

Substituting (19) into (18), one can obtain $\boldsymbol{x}_{\mathrm{n}}$ as

$$\boldsymbol{x}_{\mathrm{n}} = \left(\boldsymbol{E} - \boldsymbol{\Phi}\left(\boldsymbol{\kappa}_{\mathrm{n}}\right)\right)^{-1}\boldsymbol{\Omega}\left(\boldsymbol{\kappa}_{\mathrm{n}}, \boldsymbol{U}\right). \tag{20}$$

Based on the analysis in Section II-B, there are 64 possible switching sequences in the full-mode operation during period $T_{\mathrm{max\_com}}$. To obtain the general solutions of the full-mode discrete-time mapping, matrix $\boldsymbol{M}_i$ is rewritten as $\boldsymbol{M}_i = [\boldsymbol{M}_{11}\ \boldsymbol{M}_{12}; \boldsymbol{M}_{21}\ \boldsymbol{M}_{22}; \boldsymbol{M}_{31}\ \boldsymbol{M}_{32}; \boldsymbol{M}_{41}\ \boldsymbol{M}_{42}]$ and uniformly expressed as

$$\begin{aligned}\boldsymbol{M}_{11\_\mathrm{XPPNXX}} &= \boldsymbol{M}_{11\_\mathrm{XPNPXX}} = \boldsymbol{M}_{11(\mathrm{A})} \\ \boldsymbol{M}_{11\_\mathrm{XPPPXX}} &= \boldsymbol{M}_{11\_\mathrm{XPNNXX}} = \boldsymbol{M}_{11(\mathrm{B})} \\ \boldsymbol{M}_{11\_\mathrm{PNXXXX}} &= \boldsymbol{M}_{11\_\mathrm{NNXXXX}} = \boldsymbol{0} \\ \boldsymbol{M}_{21\_\mathrm{XXPNXX}} &= -\boldsymbol{M}_{21\_\mathrm{XXNPXX}} = \boldsymbol{M}_{21} \\ \boldsymbol{M}_{21\_\mathrm{XXPPXX}} &= -\boldsymbol{M}_{21\_\mathrm{XXNNXX}} = \boldsymbol{0}. \end{aligned}$$

$\boldsymbol{M}_{12}, \boldsymbol{M}_{22}, \boldsymbol{M}_{31}, \boldsymbol{M}_{32}, \boldsymbol{M}_{41}$, and $\boldsymbol{M}_{42}$ remain unchanged during the full-mode operation.

TABLE VI
PARAMETERS OF THE FSBB-IPT SYSTEM

Parameters	Values	Parameters	Values
L	55 μH	L_1	75.7 μH
C_{f}	5 μF	L_2	77.5 μH
L_{p}	41.5 μH	C_1	102.5 nF
L_{s}	41.5 μH	C_2	97.4 nF
C_{p}	83.7 nF	ε	4.25/2.215/1
C_{s}	84.5 nF	f_{N}	85 kHz

TABLE VII
COMPARISON IN BUCK MODE

Response	ε	Q_{fitness} (%)		
		FHA	DTM [14]	TTSM
i_{L}	4.25	74.12	86.30	98.84
	2.125	76.44	88.84	99.01
	1	77.87	90.23	98.69
i_{p}	4.25	88.48	91.60	99.05
	2.125	90.03	90.11	98.93
	1	91.56	89.38	99.20
i_{s}	4.25	87.78	92.66	99.09
	2.125	84.62	91.64	98.87
	1	86.22	92.71	98.82

The input matrix $\boldsymbol{N}_i = [\boldsymbol{N}_1; \boldsymbol{N}_2]$ is expressed as

$$\begin{aligned}\boldsymbol{N}_{1\_\mathrm{PPXXXX}} &= \boldsymbol{N}_{1\_\mathrm{PNXXXX}} = \boldsymbol{N}_1 \\ \boldsymbol{N}_{1\_\mathrm{NPXXXX}} &= \boldsymbol{N}_{1\_\mathrm{NNXXXX}} = \boldsymbol{0} \\ \boldsymbol{N}_{2\_\mathrm{XXXXPN}} &= -\boldsymbol{N}_{2\_\mathrm{XXXXNP}} = \boldsymbol{N}_2 \\ \boldsymbol{N}_{2\_\mathrm{XXXXPP}} &= \boldsymbol{N}_{2\_\mathrm{XXXXNN}} = \boldsymbol{0}. \end{aligned}$$

The detailed expressions of $\boldsymbol{M}_i$ and $\boldsymbol{N}_i$ are given in the Appendix.

C. Comparison With Other Models

To illustrate the superiority of TTSM applied to systems containing multiple time-scale variables, Fig. 11 compares the results of fundamental harmonic approximation (FHA) [29], DTM in [14], time-domain simulations, and TTSM when the cascaded system operates at different ε. In the case of FHA, it is unable to simultaneously solve for time-domain variables at different operating frequencies; therefore, the results are obtained by decoupling the cascaded system. When applying the DTM with a single time scale, the resonant period T_{N} is chosen as the reference time scale to obtain more mapping points.

The system parameters are listed in Table VI. An accuracy index Q_{fitness}, which is defined in (21), is used to quantize the model accuracy. In this article, the observations in 10^2 full-mode operating periods are used for the comparative study.

$$Q_{\mathrm{fitness}} = \left(1 - \frac{\| A - \hat{A}\|_2}{\| \hat{A} - \mathrm{mean}\left\{\hat{A}\right\}\|_2}\right) \times 100\%. \tag{21}$$

In (21), A is the calculated results of different models, and $\hat{A}$ is the true system output. Tables VII–IX present the accuracy performance of different models.

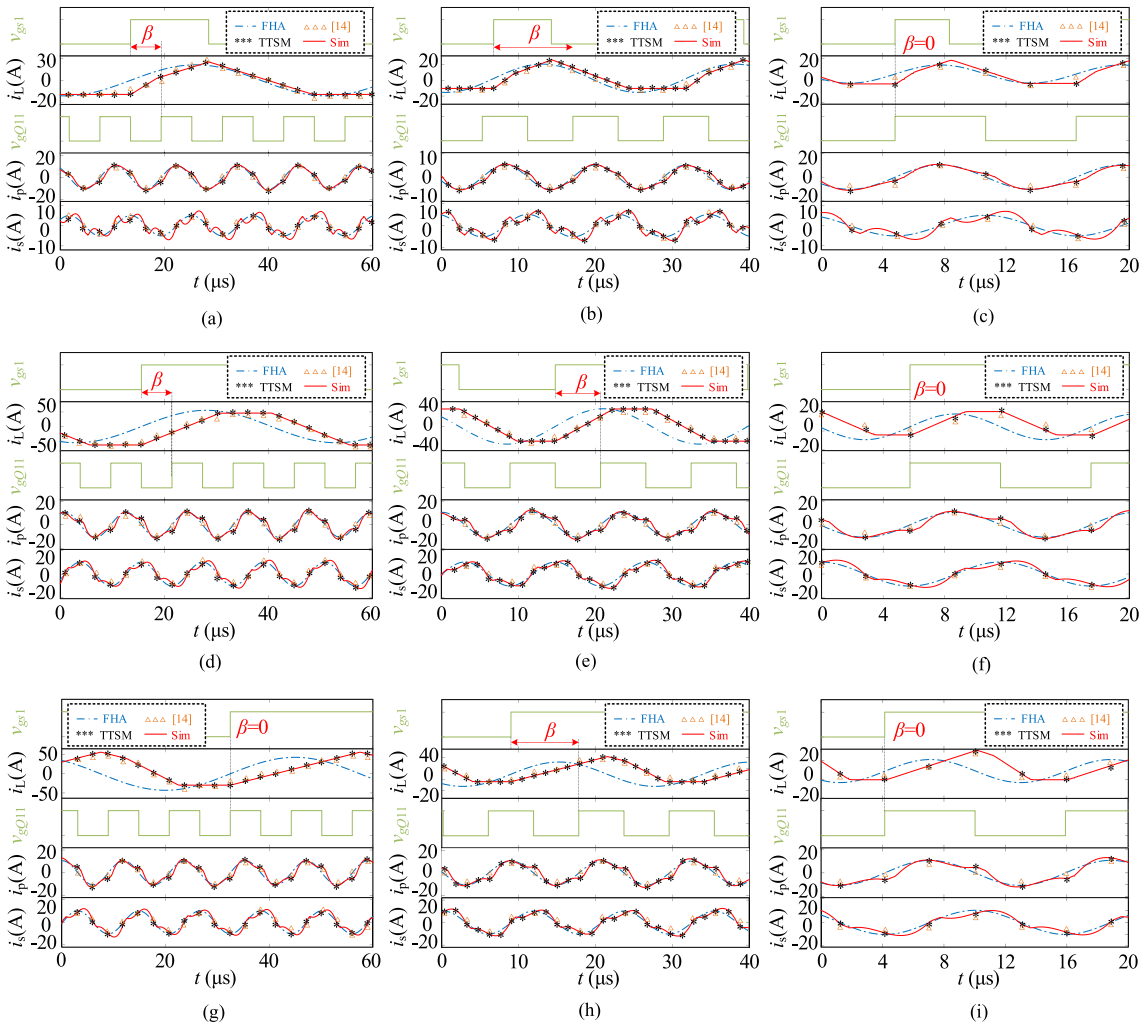

Fig. 11. Model verification. (a) Buck mode, $\varepsilon = 4.25$. (b) Buck mode, $\varepsilon = 2.125$. (c) Buck mode, $\varepsilon = 1$. (d) Equal mode, $\varepsilon = 4.25$. (e) Equal mode, $\varepsilon = 2.125$. (f) Equal mode, $\varepsilon = 1$. (g) Boost mode, $\varepsilon = 4.25$. (h) Boost mode, $\varepsilon = 2.125$. (I) Boost mode, $\varepsilon = 1$. (a) $d_1 = 0.3, d_2 = 0.6, \alpha = 0.1$. (b) $d_1 = 0.3, d_2 = 0.6, \alpha = 0.1$. (c) $d_1 = 0.3, d_2 = 0.6, \alpha = 0.1$. (d) $d_1 = 0.5, d_2 = 0.5, \alpha = 0.3$. (e) $d_1 = 0.5, d_2 = 0.5, \alpha = 0.3$. (f) $d_1 = 0.5, d_2 = 0.5, \alpha = 0.3$. (g) $d_1 = 0.6, d_2 = 0.3, \alpha = 0.4$. (h) $d_1 = 0.5, d_2 = 0.5, \alpha = 0.4$. (i) $d_1 = 0.5, d_2 = 0.5, \alpha = 0.4$.

TABLE VIII
COMPARISON IN EQUAL MODE

Response	ε	Q_{fitness} (%)		
		FHA	DTM [14]	TTSM
i_{L}	4.25	66.98	91.25	98.75
	2.125	60.57	91.56	99.07
	1	61.76	89.47	99.02
i_{p}	4.25	83.79	89.95	98.48
	2.125	85.93	87.66	98.46
	1	82.56	87.54	99.22
i_{s}	4.25	80.64	88.69	98.54
	2.125	87.05	90.68	99.16
	1	86.29	90.39	98.43

TABLE IX
COMPARISON IN BOOST MODE

Response	ε	Q_{fitness} (%)		
		FHA	DTM [14]	TTSM
i_{L}	4.25	55.43	93.49	98.22
	2.125	48.84	92.15	98.52
	1	52.16	92.44	99.03
i_{p}	4.25	85.34	90.80	98.27
	2.125	86.78	90.81	98.80
	1	85.76	87.42	99.10
i_{s}	4.25	88.41	92.37	98.62
	2.125	83.97	90.05	98.54
	1	84.84	91.56	98.63

The discrete-time mapping starts from the reference starting point of the full-mode period. The results in Fig. 11 show that the mapping points of variables i_{L}, i_{p}, and i_{s} are synchronously corresponding in time sequence. When $\varepsilon = 1$, the FSBB-IPT system has a single time scale and the TTSM is equivalent to periodic mapping to display the accuracy of TTSM, and the time scale in Fig. 11(c), (f), and (i) is chosen as half of the original time scale.

In boost mode, the ZVS current of the first stage is relatively small and i_{L} contains a significant dc bias alongside its

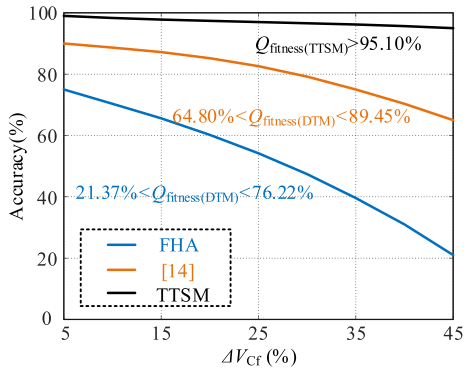

Fig. 12. Comparison of FHA, DTM [14], and TTSM in accuracy with different ΔV_{Cf}.

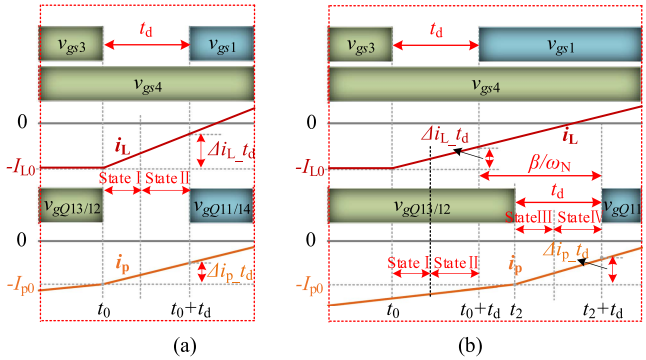

Fig. 13. Zoom-in waveforms of the FSBB-IPT system in the dead time. (a) $\beta = 0$. (b) $\beta \neq 0$.

fundamental component. As a result, the accuracy of FHA is much lower. Regarding the DTM in [14], through mapping observation, especially during the transitions in the full-mode operation, it was observed that the results deviate significantly from the true system responses, which is mainly due to its oversight of changes in operating states and the absence of mode rearrangement.

In Fig. 11(c), (f), and (i), when the two stages operate at the same frequencies (i.e., $\varepsilon = 1$), which means that only one time scale exists in the cascaded system, β is always zero. The synchronous modulation of the two cascaded stages can be easily achieved. In the case of Fig. 11(a), (b), (d), and (e), the hybrid ZVS modulation scheme conducted in the new time scale will be introduced in Section IV. It is important to note that in Fig. 11(g), when $\beta = 0$, it does not imply the absence of the modulation synchronization issue. Rather, it simply means that this moment marks the beginning of the full-mode period $T_{\max\_com}$.

TTSM considers the bus capacitor C_f in the variables, making it suitable for general nonfully decoupled cascaded systems or independent multi-time-scale systems. Fig. 12 presents the model results under different levels of voltage ripple. It can be observed that when the capacitance value is smaller, indicating lower decoupling and larger voltage ripple, TTSM still maintains a high level of accuracy (>95%), whereas the accuracies of FHA and DTM decrease significantly as the coupling decreases.

D. Extension to Other Scenarios

This article exclusively focuses on the discussion of the cascaded FSBB-IPT system to present the TTSM. In fact, it can apply to various systems, including cascaded IPT systems, cascaded nonisolated converters, etc. When researching other systems, it is important to consider the following matters:

1) for cascaded or interleaved systems operating at different frequencies, the calculated minimum common period T_m could be particularly small. In such cases, T_m only needs to be greater than or equal to the dead time t_d to meet the model accuracy requirements;

2) in the full-mode operation of the cascaded system, there could be instances where the duration of a particular state is shorter than the dead time. It is permissible to disregard this state to reduce the complexity of model derivation;

3) when the capacitance of the bus capacitor is large enough, the two cascaded stages will be decoupled completely, it could be more convenient to study the two stages by using the single-time-scale models.

IV. Hybrid ZVS Modulation

A. ZVS Conditions and Inductor RMS Current

In practice, the currents in the dead time are usually nonlinear; however, some researchers treat it as constant [11], or only one mode is considered [24], resulting in low accuracy in obtaining ZVS conditions. To obtain more precise ZVS conditions, as shown in Fig. 13, the inductor current i_L and inverter current i_p increase linearly during the dead time and can be divided into two modes. $-I_{L0}$ is the valley current of i_L. Δi_{L_td} and Δi_{p_td} represent the variations of i_L and i_p in the dead time, respectively.

In state I, the inductor current i_L discharges the paralleled output capacitor C_{oss1} of S_1 and charges the paralleled output capacitor C_{oss3} of S_3, and the inverter current i_p discharges the capacitor C_{11} of Q_{11} and charges the capacitor C_{13} of Q_{13}. State I will finish when C_{oss1} and C_{11} are discharged completely, which means $v_{ds1} = 0$ and $v_{ds11} = 0$. By using the linearization approximation, i_L and i_p are increased linearly in state II. $C_{oss} = C_{oss1} = C_{oss2} = \ldots = C_{11} = C_{12} = \ldots = C_{24}$ due to the adoption of the same MOSFETs. In the full-mode operating period, because of the presence of phase shift β, it is necessary to consider the synchronization issue of modulation when $f_M \neq f_N$.

To achieve the ZVS of S_1 and Q_{11}, the duration time of states I and III should be shorter than the dead time t_d, by using (1), thus the ZVS conditions of S_1 and Q_{11} can be expressed as

$$V_{in}t_d/L + 2C_{oss}V_{in}/t_d \leq I_{L0} \tag{22}$$

$$2\sigma C_{oss}V_{in}/t_d \leq I_{p0} \tag{23}$$

where $2C_{oss}V_{in}/t_d$ and $I_{p\_ZVS} = 2\sigma C_{oss}V_{in}/t_d$ are the total charge of the output capacitors of S_1 and Q_{11}, respectively.

Similarly, the ZVS conditions of S_2, S_3, and S_4 can be obtained as

$$(\sigma - 1)V_{in}t_d/(2L) + 2\sigma C_{oss}V_{in}/t_d \leq I_{L1} \tag{24}$$

$$\sigma V_{\text{in}} t_{\text{d}}/L + 2C_{\text{oss}} V_{\text{in}}/t_{\text{d}} \le I_{\text{L2}} \tag{25}$$

$$2\sigma C_{\text{oss}} V_{\text{in}}/t_{\text{d}} \le I_{L0}, t_{\text{M4}} \ge t_{\text{d}} \tag{26}$$

where I_{L1}, I_{L2}, and t_{M4} are shown in Fig. 2. When $\sigma > 1$, $I_{\text{L1}} < I_{\text{L2}}$, and when $\sigma < 1$, $I_{\text{L1}} > I_{\text{L2}}$.

Based on the analysis mentioned above, the ZVS conditions can be unified as

$$\begin{cases} 2C_{\text{oss}} \max\{V_{\text{in}}, \sigma V_{\text{in}}\}/t_{\text{d}} + V_{\text{in}} t_{\text{d}}/L \le I_{\text{L0}} \\ 2C_{\text{oss}} \max\{V_{\text{in}}, \sigma V_{\text{in}}\}/t_{\text{d}} + \sigma V_{\text{in}} t_{\text{d}}/L \le \min\{I_{L1}, I_{L2}\} \\ t_{\text{d}} \le t_{\text{M4}} \\ 2\sigma C_{\text{oss}} V_{\text{in}}/t_{\text{d}} \le I_{\text{p0}} \end{cases} \tag{27}$$

where $I_{\text{L\_ZVS}} = 2C_{\text{oss}} \max\{V_{\text{in}}, \sigma V_{\text{in}}\} + \sigma V_{\text{in}} t_{\text{d}}/L$ is the minimum current of I_{L1} and I_{L2} to fully discharge the paralleled output capacitors.

According to the full-mode operation in Section II, t_{M1} and t_{M3} can be obtained as

$$t_{\text{M1}} = (I_{\text{L1}} - I_{\text{L0}})\, L/V_{\text{in}}, t_{\text{M3}} = (I_{\text{L1}} - I_{\text{L0}})\, L/\sigma V_{\text{in}}. \tag{28}$$

The ZVS conditions (27) can further be expressed as

$$\begin{cases} I_{\text{L0}} = I_{\text{L\_ZVS}} = 2C_{\text{oss}} \max\{V_{\text{in}}, \sigma V_{\text{in}}\}/t_{\text{d}} + V_{\text{in}} t_{\text{d}}/L \\ t_{\text{M1}} \ge t_{\text{M1\_ZVS}} = 4C_{\text{oss}} L/t_{\text{d}} + (1+\sigma)\, t_{\text{d}}, \quad \sigma \le 1 \\ t_{\text{M3}} \ge t_{\text{M3\_ZVS}} = 4C_{\text{oss}} L/t_{\text{d}} + (1+\sigma)\, t_{\text{d}}/\sigma, \sigma > 1 \\ t_{\text{M4}} = t_{\text{M4\_min}} \ge t_{\text{d}} \\ I_{\text{p0}} \ge I_{\text{p0\_ZVS}} = 2\sigma C_{\text{oss}} V_{\text{in}}/t_{\text{d}}. \end{cases} \tag{29}$$

By the elimination of the variables t_{M3}, t_{M4}, I_{L1}, and I_{L2} [12], t_{M1}, t_{M2} can be chosen as the modulation variables of the cascaded system to achieve the ZVS and reduced the inductor current $I_{\text{L\_RMS}}$, which is

$$\begin{aligned} I_{\text{L\_RMS}} &= \sqrt{f_{\text{M}} \int_{t_0}^{t_0+T_{\text{M}}} i_{\text{L}}(t)\, dt} \\ &= I_{\text{L\_RMS}}(t_{\text{M1}}, t_{\text{M2}}, I_{L0}, V_{\text{in}}, \sigma) \end{aligned} \tag{30}$$

where the detailed expression is shown in the Appendix.

B. Proposed Hybrid Modulation Scheme

In the three-mode and four-mode modulation schemes [11], [12], [22], [23], [24], [25], [26], four time segments t_{M1}–t_{M4} are selected as the variables to minimize the $I_{\text{L\_RMS}}$. To mitigate variations in the sampling frequencies and calculation discrepancies between the cascaded stages, a hybrid ZVS modulation scheme in terms of the phase shift β in the new time scale T_{m} is proposed, where the sampling frequency f_{m} is constant. The hybrid modulation scheme is conducted in the full-mode operating period $T_{\text{max\_com}}$, which has the following advantages: 1) the adoption of a constant sampling frequency mitigates the challenges stemming from the differences between the operating frequencies of the cascaded stages; 2) reselection of the modulation variables is avoided, enabling the ZVS operation in wide voltage range.

Fig. 14 gives the control diagram of the FSBB-IPT system with the hybrid modulation scheme, where the phase shift γ serves as the modulation variable for the second-stage IPT system. The constraints of modulation variables t_{M1}, t_{M3}, and t_{M4} can be easily obtained according to (29), and t_{M2} can be defined as the output of the PI controller, which is noted as $t_{\text{M2\_PI}}$. The output signal $t_{\text{M3\_End}}$ from the comparator functions as an indicator for the switching state of S_3. Specifically, when the detected current i_{L} falls below the threshold $-I_{\text{L\_ZVS}}$, S_3 switches ON, while S_4 switches OFF. The current i_{L} is rerouted through the reverse antiparallel diode of S_3 for continued conduction. t_{M4} can be dynamically adjusted to ensure a constant period of the first stage. The comparison between i_{p} and $I_{\text{p\_ZVS}}$ is used to determine whether the inverter in the second stage is operating under ZVS conditions. Moreover, the minimum value of $I_{\text{L\_RMS}}$ varies monotonically with I_{L1} and I_{L2} when $\sigma > 1$ and $0 < \sigma \le 1$, respectively [26]. The minimum I_{L1} and I_{L2} are both $I_{\text{L\_ZVS}}$.

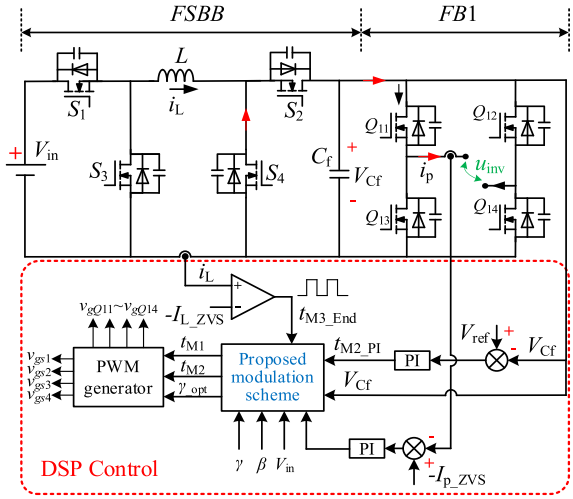

Fig. 14. Modulation diagram of the cascaded FSBB-IPT system.

Thus, the time segment t_{M1} and phase shift γ are the modulation variables need to be optimized. As analyzed in Sections II and III, the time sequences in the fast and slow time scale can be transferred into new time scale T_{m}, which makes it possible to achieve ZVS modulation without changing the sampling frequency.

The proposed modulation scheme for the system can be given as

$$t_{\text{M1}} = t_{\text{M1\_ZVS}} + f(T_m) + f(\beta) \tag{31}$$

where $f(T_{\text{m}}) = k_1 T_{\text{m}}$ is a monotonic function and always greater than zero. $f(\beta) = k_2 \beta$ is an adjustment function, which facilitates the realization of the modulation synchronization of the variables t_{M1} and γ in period $T_{\text{max\_com}}$. k_1 and k_2 are obtained offline. For each possible $\beta|_{T\text{m}}$ ($\beta|_{T\text{m}}$ means that β is expressed in new time scale T_{m}), k_2 possesses uniqueness.

In instances of light loads, $f(T_{\text{m}})$ needs to be a relatively small value, potentially converging to zero, and under heavy loads, $f(T_{\text{m}})$ should provide substantially larger values. Moreover, it is crucial that $f(T_{\text{m}})$ permits continuous modulation, thereby avoiding resection of the modulation variables.

Fig. 15 shows the principle of the proposed modulation scheme. The shadow areas shown in Fig. 15 represent the power

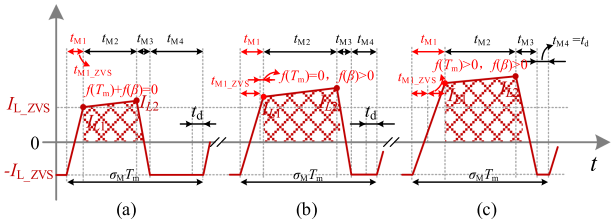

Fig. 15. Principle of the proposed hybrid modulation scheme, $0 < \sigma \leq 1$.

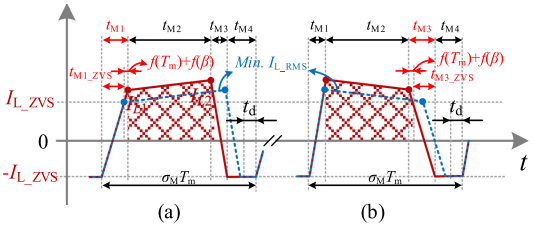

Fig. 16. Modulation variable selection. (a) $0 < \sigma \leq 1$. (b) $\sigma > 1$.

transfer ability of the first stage. It is obvious that t_{M2} increases with the output power, while t_{M4} decreases to keep the T_M constant. When t_{M4} decreases to t_d, the FSBB converter begins to enter CCM operation.

As shown in Fig. 16, t_{M1} and t_{M3} are the variables to be discussed in buck and boost modes, respectively. The value of inductor current I_{L_RMS} exhibits a strong correlation with I_{L1} and I_{L2} when $0 < \sigma \leq 1$ and $\sigma > 1$. The minimum of I_{L_RMS} occurs at the time when $I_{L1} = I_{L\_ZVS}$ in buck mode and $I_{L2} = I_{L\_ZVS}$ in boost mode, respectively. When the load power P_o is lower than the rated power P_{o_rated}, the constraint $t_{M4} \geq t_d$ is readily achievable. Throughout the modulation process, it is imperative to consistently satisfy the condition where t_{M4} is greater than t_d.

When the first stage operates in the buck mode to meet the requirements mentioned above, $f(T_m)$ is defined as $(n + a)T_m$ in this article, (31) can further be expressed as

$$t_{M1} = t_{M1\_ZVS} + (n + a)\, T_m + f\,(\beta) \tag{32}$$

where $n = 0, 1, 2, \ldots, 0 < a < 1$. n is used to achieve rapid adjustment of t_{M1}, and a ensures its precision. With the help of volts-second balance of the inductor L, one can obtain the unified expression of the proposed modulation scheme of the first stage when $0 < \sigma \leq 1$, which is

$$t_{M1} = t_{M1\_ZVS} + (n + a)\, T_m \tag{33}$$

$$t_{M3} = (t_{M1\_ZVS} + (n + a)\, T_m)\, /\sigma + (1 - \sigma) t_{M2}/\sigma. \tag{34}$$

Similarly, when $\sigma > 1$, one can obtain the variables as

$$t_{M1} = \sigma\,(t_{M3\_ZVS} + (n + a)\, T_m) - (1 - \sigma) t_{M2}/\sigma \tag{35}$$

$$t_{M3} = t_{M3\_ZVS} + (n + a)\, T_m. \tag{36}$$

In (33)–(36), t_{M2} is equal to t_{M2_PI}, as shown in Fig. 14, which is utilized for adjusting the voltage gain of the first stage. t_{M4} is always greater than the dead time t_d. It is noticed that $f(\beta)$ is delineated as a "global parameter" that does not directly

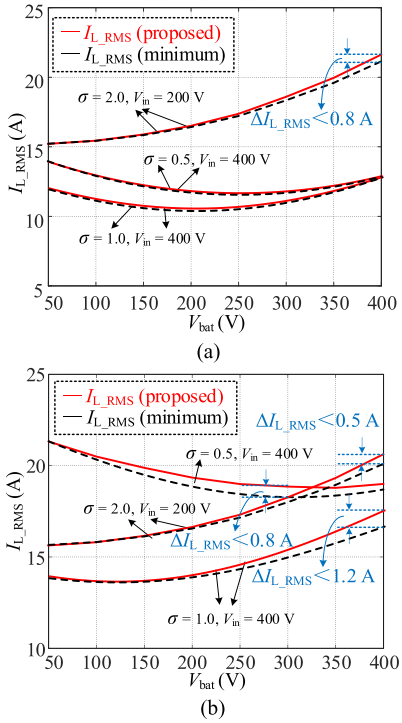

Fig. 17. Relationship between I_{L_RMS} and battery voltage V_{bat} with different n when $a = 0.1$, $k = 0.2$. (a) $n = 2$. (b) $n = 4$.

participate in specific steps during the process of $f(T_m)$ calculation. After the execution of calculation processes for t_{M1}–t_{M4} within the period $\sigma_M T_m$, $f(\beta)$ is employed as an adjustment factor for the realization of synchronous modulation between the two cascaded stages. If $\beta = 0$, $f(\beta)$ is not required.

When $t_{M4} = t_d$, by combining (9) and (29) with (33)–(36), one can obtain

$$\mathbf{\Gamma}\,(n + a, T_m, \sigma, L, \sigma_M) = 0 \tag{37}$$

where T_m, σ_M, and L are known parameters. The value of $n+a$ corresponds uniquely with the voltage gain σ. When n is an integer, a is naturally obtained. It is obvious that $0 \leq n < \sigma_M$.

Given the parameters as: $f_M = 40$ kHz, $f_N = 85$ kHz, $L = 55$ μH, $t_d = 300$ ns, and $C_{oss} = 180$ pF. The comparison of $I_{L\_RMS(prop)}$ when adopting the proposed modulation scheme and the minimum of $I_{L\_RMS(min)}$ is shown in Fig. 17. It can be observed from Fig. 16 that when $n = 0$, $I_{L\_RMS(prop)}$ is always equal to $I_{L\_RMS(min)}$. In Fig. 17(a), when $n = 2$, and the voltage gain $0 < \sigma \leq 1$, the curves of $I_{L\_RMS(prop)}$ and $I_{L\_RMS(min)}$ are highly consistent, with negligible error. When $n = 2$ and $\sigma = 2$, the maximum derivation of I_{L_RMS} does not exceed 0.8 A. When $n = 4$, as shown in Fig. 17(b), the maximum deviations in the three operating modes are 0.5 A, 1.2 A, and 0.8 A, respectively. The results show that the modulation scheme in the new time scale can effectively reduce I_{L_RMS}.

Fig. 18 shows the relationship between the maximum inductor current error $\Delta I_{L\_RMS\_max}$ and the value of a. It can be observed from Fig. 18 that when $n = 4$, $\Delta I_{L\_RMS\_max}$ is positively correlated with a and the maximum of $\Delta I_{L\_RMS\_max}$

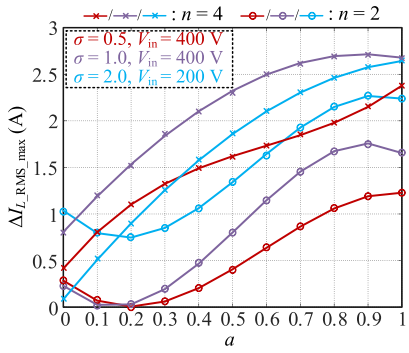

Fig. 18. Relationship between $\Delta I_{\mathrm{L\_RMS\_max}}$ and a with different n.

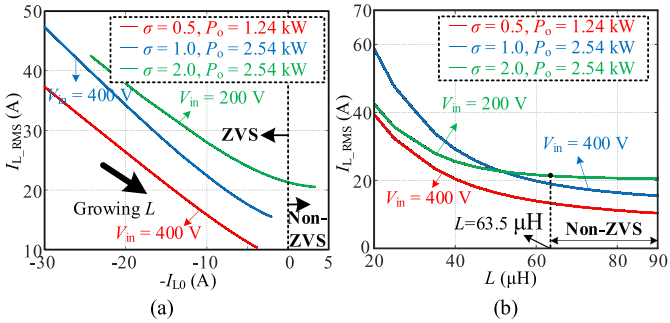

Fig. 20. Relationship between $I_{\mathrm{L\_RMS}}$ and I_{L0} with different σ when $f_{\mathrm{M}} = 40$ kHz, $V_{\mathrm{bat}} = 400$ V, and $k = 0.2$.

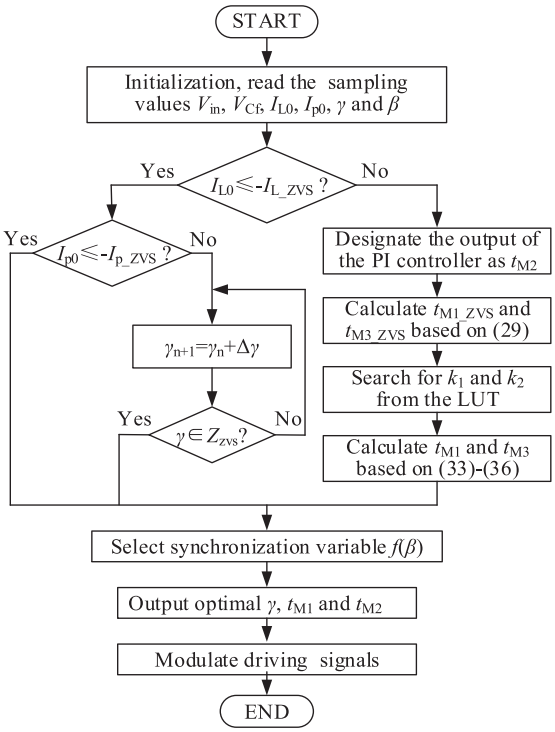

Fig. 19. Flowchart of the hybrid ZVS modulation.

is smaller than 2.7 A. When $n = 2$, there is an inflection point at approximately $a = 0.2$, at which the maximum current error $\Delta I_{\mathrm{L\_RMS\_max}}$ is minimized. Furthermore, it can be observed that the maximum current errors when $n = 4$ are generally greater than the calculated results when $n = 2$, which indicates that the parameter n has a more significant impact on the results of the modulation strategy.

C. Implementation Flowchart

The implementation flowchart of the proposed hybrid modulation strategy is shown in Fig. 19. The output voltage of the FSBB converter is sampled first, thus the operating mode ($\sigma > 1$, $0 < \sigma < 1$, or $\sigma = 1$) can be easily determined. γ_{n} and $\gamma_{\mathrm{n+1}}$ are the phase shifts between the primary and secondary inverters in n_{th} and $(n+1)_{\mathrm{th}}$ iteration cycle, respectively. $\Delta\gamma$ is the iteration step for achieving the ZVS operation of the second stage, and it is defined as 0.001 rad/s in this article. Z_{ZVS} represents the ZVS operation range with respect to phase shift γ, which can be obtained based on the analysis in [30]. The LUT for $k_1 = n+a$ obtained offline is stored in DSP TMS320F28335.

D. Design of the Inductor

The power transfer ability of the first stage relies on both the performance of MOSFETs and the inductance L. To reduce the current stress on the switches and achieve ZVS operation within a wide voltage range, it is crucial to strike a balance between the inductance L and RMS value $I_{\mathrm{L\_RMS}}$ of the inductor.

Fig. 20(a) presents the relationship between the RMS value $I_{\mathrm{L\_RMS}}$ of the inductor current and $-I_{\mathrm{L0}}$ when the FSBB converter operates in three modes. It can be observed that $I_{\mathrm{L\_RMS}}$ has an approximate linear relationship with $-I_{\mathrm{L0}}$. Moreover, as the value of the inductance increases, the absolute value of $-I_{\mathrm{L0}}$ decreases, making it more challenging to achieve ZVS within a wide voltage range. Fig. 20(b) shows the relationship between $I_{\mathrm{L\_RMS}}$ and L. The value of $I_{\mathrm{L\_RMS}}$ decreases with increasing inductance L. Specifically, when $20\ \mu\mathrm{H} < L < 50\ \mu\mathrm{H}$, the current decreases rapidly, indicating that within this range, the inductance L has a significant impact on the current. When the inductance exceeds 50 μH, the current variation is relatively gradual, which is more conducive to the safe operation of the converter. However, when the voltage gain σ is 2 and the inductance exceeds 63.5 μH, the first stage will begin to enter non-ZVS operating region. Thus, the selection of inductor values in this article is constrained within the range of 50–63.5 μH.

Fig. 21 shows the relationship between $I_{\mathrm{L\_RMS}}$ and the operating frequency f_{M} of the first stage. Similar to the relationship between $I_{\mathrm{L\_RMS}}$ and L, $I_{\mathrm{L\_RMS}}$, the curve exhibits a point of inflection around $f_{\mathrm{M}} = 30$ kHz, beyond which, as the operating frequency increases, the current variation becomes more gradual. For the cascaded FSBB-IPT system, the first stage is more suitable for operating in frequency ranges above 30 kHz.

Considering the capacity of switches and system parameter design, the inductor value is selected as 55 μH, and the operating frequency of the first stage is defined as 40 kHz.

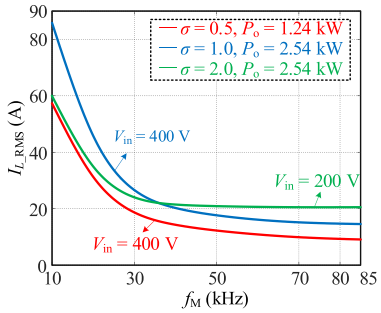

Fig. 21. Relationship between $I_{\mathrm{L\_RMS}}$ and f_{M} with different σ when $L = 55$ μH, $V_{\mathrm{bat}} = 400$ V, and $k = 0.2$.

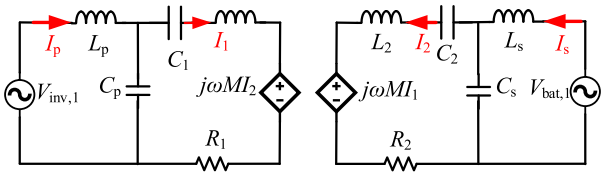

Fig. 22. Simplified equivalent circuit of the second-stage IPT system.

E. Maximum Efficiency Tracking

Fig. 22 shows the equivalent circuit of the *LCC–LCC* compensated IPT system. R_1 and R_2 represent the equivalent series resistances of the transmitter and receiver coils, respectively. The power losses in the ferrite plates that shield the coils and the equivalent series resistances of the passive components are negligible. $V_{\mathrm{inv},1}$ and $V_{\mathrm{bat},1}$ are the fundamental output voltages of FB1 and FB2 and the desired input voltage V_{Cf} of the inverter FB1 is achieved by adjusting the duty cycles d_1 and d_2 of the FSBB converter. One can obtain $V_{\mathrm{inv},1}$ and $V_{\mathrm{bat},1}$ as [31]

$$\dot{V}_{\mathrm{inv},1} = \frac{2\sqrt{2}}{\pi} V_{Cf} \sin\left(\frac{\varphi_1}{2}\right) = \frac{2\sqrt{2}\sigma}{\pi} V_{\mathrm{in}} \sin\left(\frac{\varphi_1}{2}\right) \tag{38}$$

$$\dot{V}_{\mathrm{bat},1} = \frac{2\sqrt{2}}{\pi} V_{\mathrm{bat}} \sin\left(\frac{\varphi_2}{2}\right) \angle -\gamma. \tag{39}$$

Assuming that the parameters of the resonant tank are symmetrical, thus the transferred power can be calculated as

$$P_{\mathrm{o}} = \mathrm{Re}\left\{-\dot{V}_{\mathrm{bat},1}\dot{I}_{\mathrm{s}}^{*}\right\} = \frac{\alpha k}{X} V_{\mathrm{inv},1} V_{\mathrm{bat},1} \sin(\gamma) \tag{40}$$

where $\alpha = L_1/L_{\mathrm{p}} = L_2/L_{\mathrm{s}}$, $X = \omega L_{\mathrm{p}} = 1/\omega C_{\mathrm{p}} = \omega L_{\mathrm{s}} = 1/\omega C_{\mathrm{s}}$, and $\sigma = d_1/d_2$.

By neglecting the switching losses, the overall power losses of the cascaded FSBB-IPT system can be given as

$$P_{\mathrm{loss}} = I_1^2 R_1 + I_2^2 R_2 = \left(V_{\mathrm{inv},1}^2 + V_{\mathrm{bat},1}^2\right) R/X^2 \tag{41}$$

where $R_1 = R_2 = R$.

The system efficiency can be calculated as

$$\eta = P_{\mathrm{o}}/\left(P_{\mathrm{o}} + P_{\mathrm{loss}}\right) = \frac{\alpha k X \sin(\gamma)}{\alpha k X \sin(\gamma) + \left(\frac{V_{\mathrm{inv},1}}{V_{\mathrm{bat},1}} + \frac{V_{\mathrm{bat},1}}{V_{\mathrm{inv},1}}\right) R}. \tag{42}$$

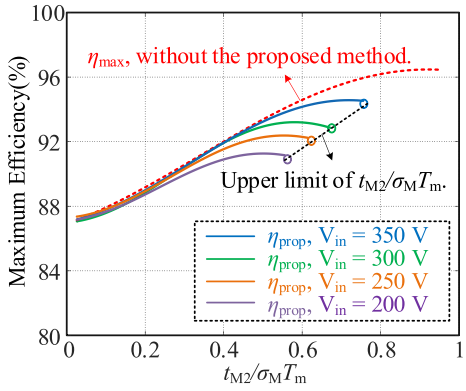

Fig. 23. Curves of $\eta_{\max}$ and η_{prop} with respect to $t_{\mathrm{M2}}/(\sigma_{\mathrm{M}} T_{\mathrm{m}})$ when $f_{\mathrm{M}} = 40$ kHz, $n = 2$, and $a = 0$.

By denoting $V_{\mathrm{inv},1}/V_{\mathrm{bat},1}$ as Ω, one can obtain the optimal condition for maximum efficiency by taking the derivative of $\partial\eta/\partial\Omega = 0$, which is

$$\Omega = 1. \tag{43}$$

It is obvious that to obtain the maximum efficiency of the cascaded system, the output voltage V_{Cf} of the FSBB converter needs to be equal to the load voltage V_{bat}, i.e., $\sigma V_{\mathrm{in}} = V_{\mathrm{bat}}$. Theoretically, as long as the voltage gain σ varies with the load voltage, the cascaded system can always operate at the maximum efficiency. As discussed in Sections II and IV-B, the voltage gain σ can be determined as

$$\sigma = \left(t_{\mathrm{M1}} + t_{\mathrm{M2}}\right) / \left(t_{\mathrm{M2}} + t_{\mathrm{M3}}\right) \tag{44}$$

where t_{M1} and t_{M3} are given in (33)–(36) to reduce the inductor current $I_{\mathrm{L\_RMS}}$. Thus, t_{M2} can be used to adjust σ. Substituting (33)–(36) into (44), one can know that the only constraint that needs to be satisfied is $t_{\mathrm{M2}} \le \sigma_{\mathrm{M}} T_{\mathrm{m}}$-$t_{\mathrm{M1}}$-$t_{\mathrm{M3}}$-$t_{\mathrm{d}}$ when $0 < \sigma \le 1$, where t_{M4} is used to maintain the constant period $\sigma_{\mathrm{M}} T_{\mathrm{m}}$ and to match the output power requirements of the second-stage IPT system.

Similarly, one can obtain the constrain when $\sigma > 1$ as

$$\sigma^2 t_{\mathrm{M2}} - 2\sigma t_{\mathrm{M2}} + t_{\mathrm{M2}} = 0. \tag{45}$$

The unique solution of (45) is $\sigma = 1$, which is in contradiction with the given precondition that $\sigma > 1$. Therefore, when the voltage gain σ is greater than 1, the hybrid modulation strategy cannot achieve the maximum efficiency tracking of the cascaded FSBB-IPT system in the full-power range. Fig. 23 compares the theoretical maximum efficiency $\eta_{\max}$ with the efficiency η_{prop} achievable by the proposed strategy with respect to $t_{\mathrm{M2}}/(\sigma_{\mathrm{M}} T_{\mathrm{m}})$, where the rated load voltage V_{bat} is 400 V. The maximum of $t_{\mathrm{M2}}/(\sigma_{\mathrm{M}} T_{\mathrm{m}})$ can also be determined by $t_{\mathrm{M2}} \le \sigma_{\mathrm{M}} T_{\mathrm{m}}$-$t_{\mathrm{M1}}$-$t_{\mathrm{M3}}$-$t_{\mathrm{d}}$. When $t_{\mathrm{M2}}/(\sigma_{\mathrm{M}} T_{\mathrm{m}}) = 0$, there is almost no power transferred to the load and the output power P_{o} increases with $t_{\mathrm{M2}}/(\sigma_{\mathrm{M}} T_{\mathrm{m}})$, which can be known from Figs. 15 and 16, thus, the minimum of t_{M2} is limited to T_{m} for analysis. When there are no constraints on t_{M1}–t_{M4}, maximum efficiency tracking across the full-power range can be achieved by matching the voltage gain σ of the front-end FSBB converter with the load voltage V_{bat}. It can be

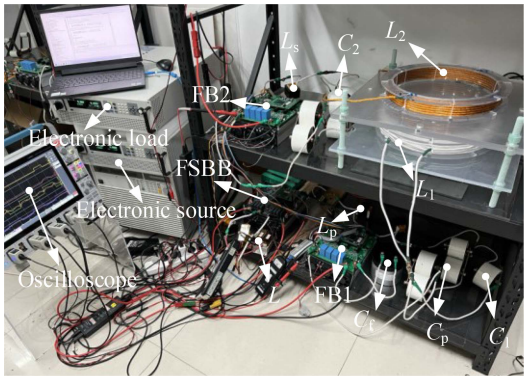

Fig. 24. Experimental prototype.

TABLE X
PARAMETERS OF THE PROTOTYPE

Parameters	Values
MOSFET	C3M0021120K C_{oss} = 180 pF @ (T_c = 25 °C, V_{DS} =1000 V), $R_{DS(on)}$ = 38 mΩ @ (V_{GS} = 15 V, I_D = 50 A, T_J = 175°C)
V_{in}	100 - 400 V
Dead time t_d	300 ns
Controller	TMS320F28335
f_M	40 kHz

observed from Fig. 23 that when $t_{M2}/(\sigma_M T_m)$ is relatively small, that is, when $0 < \sigma \leq 1$, it is possible to achieve maximum efficiency tracking. As $t_{M2}/(\sigma_M T_m)$ increases, which corresponds to the increase in P_o, the range of maximum efficiency tracking for the cascaded system decreases with the increase in voltage gain σ with the proposed scheme.

V. Experimental Verification

A. Experimental Setup

As shown in Fig. 24, an FSBB-IPT prototype is built to verify the effectiveness of the proposed hybrid modulation scheme conducted in the new time scale T_m. The main parameters of the prototype are given in Tables VI and X. When conducting the experiments, the dc link and battery packs are simulated by two bidirectional dc sources. The FSBB converter, FB1, and FB2 consist of eight parallel SiC MOSFETs (C3M0021120Ks), respectively. Experimental waveforms are measured by an oscilloscope Tektronix MSO58 8-BW-500.

B. Steady-State Operation

The waveforms of v_{ds}, v_{gs}, inductor current i_L, inverter voltage u_{inv}, and inverter current i_p in three operating modes are shown in Fig. 25. The zoom-in waveforms in the dead time are presented in Fig. 25(a-1)–(f-1). Based on the analysis in Section IV-A and the ZVS conditions in (29), the ZVS current -I_{L_zvs} of the FSBB converter can be set as −5.0 A, and the maximum ZVS current I_{p0_zvs} of the inverter is −0.5 A.

When $V_{in} > V_{Cf}$, which is presented in Fig. 25(a) and (b), the input voltage is 300 V and V_{bat} = 400 V, the output power is 1.62 kW, it can be observed that the ZVS-ON of S_1 and S_2 are achieved. At the same time, the ZVS operation of the inverter is also achieved and the ZVS currents are −1.3 A and −4.2 A, respectively.

In contrast to the operation of a single-stage converter, in three different operating modes and under various output power levels, the rate of inductor current rise during the dead time t_d varies. It increases approximately linearly rather than remaining constant, thereby validating the ZVS conditions analyzed in Section IV. Fig. 25 shows that in buck mode, the current rises most rapidly, while in equal mode, it rises more slowly. Therefore, setting I_{L_zvs} accurately is essential. In this article, $|I_{L\_zvs}|$ is difined as 5.0 A, which consistently remains greater than Δi_{L_td}, ensuring reliable achievement of ZVS for S_1.

In Fig. 25, $f(\beta)$ resolves the synchronization issue in the modulation of the two-stage converter. To enable the DSP to handle variable sampling at different time scales of the two-stage structure simultaneously and reduce computational time, the sampling frequency is defined as $f_m = 1/T_m$. In full-mode modulation, driving pulse signals from S_1 serve as triggers in full-mode period modulation, followed by delays of $f(\beta)$, $f(\beta+2\pi)$, …, to modulate the second-stage IPT system, repeating instructions every T_{max_com}. Consequently, it is clear that the steady-state waveform of the IPT system does not repeat within the period T_N, which means the operating period of the cascaded system is T_{max_com}.

Fig. 26(a), (b), (d), (e), (g), and (h) shows the waveforms of the cascaded system by adopting the proposed modulation schemes conducting in the new time scale T_m when $f(T_m) = 0$. In boost mode, as shown in Fig. 26(a) and (b), t_{M3} is equal to t_{M3_ZVS}. As the load becomes heavier, that is, the shadow area shown in Fig. 16 increases, the time segments t_{M2} increase with the output power while t_{M4} decreases. In equal mode shown in Fig. 26(d) and (e) and buck mode shown in Fig. 26(g) and (h), the operating principles are similar.

In three modes shown in Fig. 26(a), (b), (d), (e), (g), and (h), t_{M1} and t_{M3} are always fixed at the minimum values t_{M1_ZVS} and t_{M3_ZVS}, and the power transfer ability is determined by the duration time of segment t_{M2}. Therefore, the RMS value of the inductor current can be effectively minimized in the full-power range.

Fig. 26(c), (f), and (i) shows the waveforms by adopting the proposed modulation schemes when $f(T_m) > 0$. It can be seen from Fig. 26(c) that, with the shadow area increases, e.g., the output power is increasing, t_{M3} will become longer and t_{M4} decreases until it equals the dead time t_d. Under light load conditions in boost mode, $t_{M1} = t_{M1\_ZVS}$ can be consistently ensured to reduce inductor current. When $t_{M1} = t_{M1\_ZVS}$ is satisfied and t_{M4} is reduced to the dead time t_d, as the load continues to increase, t_{M3} should be calculated according to (33)–(36). Because the LUT containing the necessary values of $f(T_m)$ has been precomputed and stored offline in the DSP, it allows for quick retrieval of corresponding n and a based on the output power requirement. It significantly improves the efficiency of program execution loops. Then, by using $f(\beta)$, the

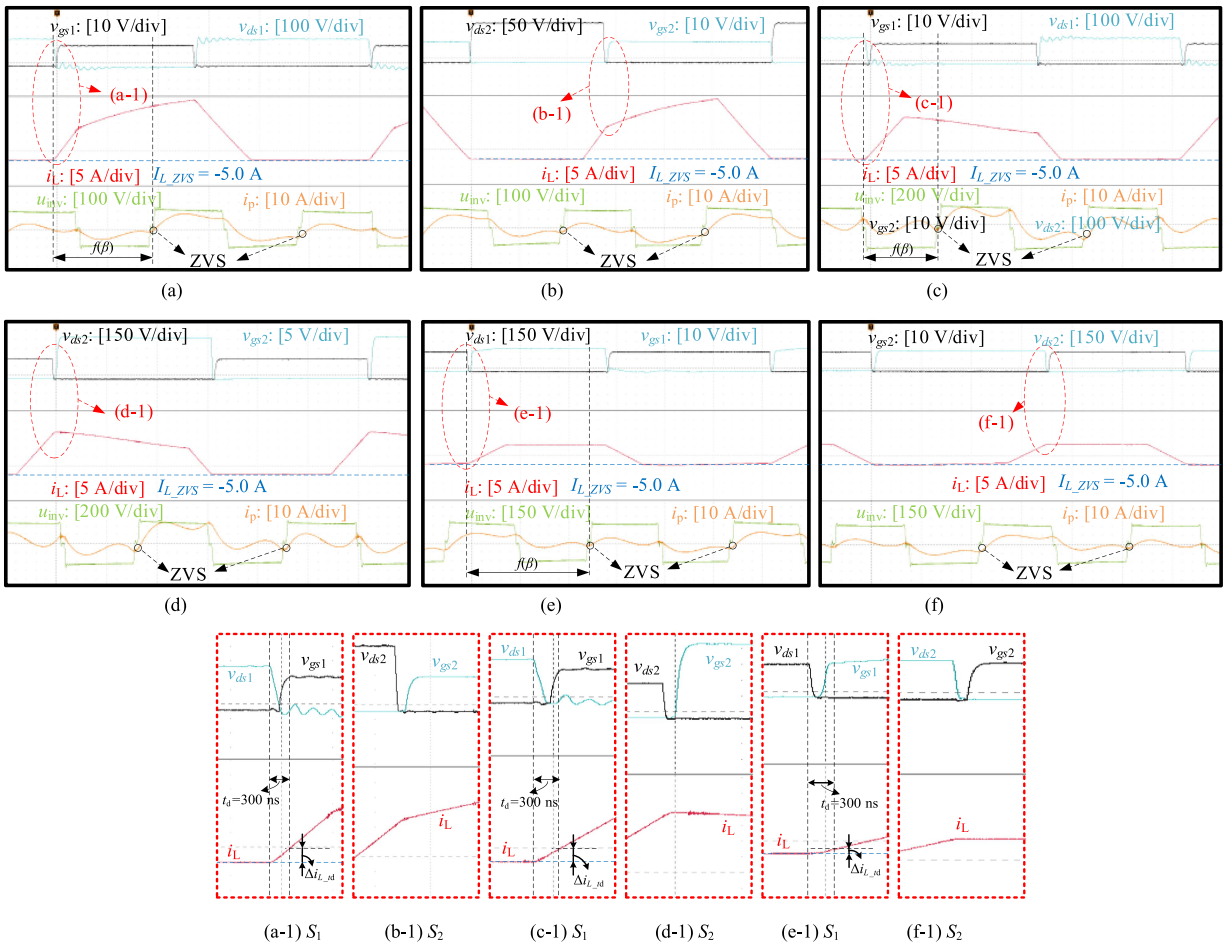

Fig. 25. ZVS waveforms of S_1 and S_2 in three modes. (a), (b) Buck mode, $V_{\rm in} = 300$ V, $V_{\rm bat} = 320$ V, $P_{\rm o} = 1.62$ kW. (c), (d) Boost mode, $V_{\rm in} = 300$ V, $V_{\rm bat} = 280$ V, $P_{\rm o} = 1.43$ kW. (e), (f) Equal mode, $V_{\rm in} = 300$ V, $V_{\rm bat} = 240$ V, $P_{\rm o} = 1.25$ kW. (a) Time: 4 μs/div. (b) Time: 4 μs/div. (c) Time: 4 μs/div. (d) Time: 4 μs/div. (e) Time: 4 μs/div. (f) Time: 4 μs/div.

required phase shift γ is obtained, facilitating the assignment of different γ in $T_{\rm max\_com}$.

In the full-power operation, the variable is sampled and calculated at the frequency $f_{\rm m}$, which can effectively reduce sampling value conversion and computational complexity. Moreover, maintaining a constant sampling frequency also is meaningful for EMI elimination.

In the proposed hybrid modulation strategy, the focus is primarily on the front-end FSBB converter and the primary-side inverter FB1 of the IPT system. As illustrated in Fig. 26, the ZVS currents of FB2 decreases as the output power $P_{\rm o}$ reduces, which means that achieving ZVS on the secondary side will be more difficult under light-load conditions.

C. Dynamic Operation

Fig. 27 shows the dynamic performance of the proposed modulation strategy at input voltage transients when $\sigma = 1$ and $V_{\rm bat} = 300$ V. As shown in Fig. 27(b), the input voltage $V_{\rm in}$ steps from 250 to 350 V, and then back to 250 V. Fig. 27(a) and (c) presents the zoom-in waveforms of the system when $V_{\rm in} = 250$ V and $V_{\rm in} = 350$ V, respectively. Similarly, the waveforms at load transitions when $\sigma = 1$ and $V_{\rm in} = 300$ V are shown in Fig. 28. The load voltage $V_{\rm bat}$ also steps from 250 to 350 V, and then back to 250 V. It can be observed from Figs. 27 and 28 that during transitions of the input voltage $V_{\rm in}$ and load voltage $V_{\rm bat}$, the responses of the system demonstrate negligible overshoot. Instead, they gradually increase or decrease along with the variations of the output power $P_{\rm o}$, which indicates that the dynamic transient is smooth with the proposed modulation scheme. The adjustment times t_{s1}–t_{s4} under input voltage transients and load voltage transients are 19.3 ms, 16.5 ms, 10.4 ms, and 9.6 ms, respectively.

Moreover, to reduce the losses during the fourth segment of the FSBB converter in the full-mode operation, the ZVS currents of the FSBB converter are consistently maintained at $|I_{\rm L\_zvs}|$, regardless of changes in loads or input voltages. By adjusting the durations $t_{\rm M1}$ and $t_{\rm M3}$, different output power requirements are met. In other words, the shadow areas illustrated in Figs. 15 and 16 will vary with the output power $P_{\rm o}$. Besides, when operating in equal mode, even with different input voltages and loads, $t_{\rm M1}$ is almost constant as long as the output power remains the same, which confirms that the proposed modulation strategy only requires a 2-D LUT to reduce the RMS value of the inductor current.

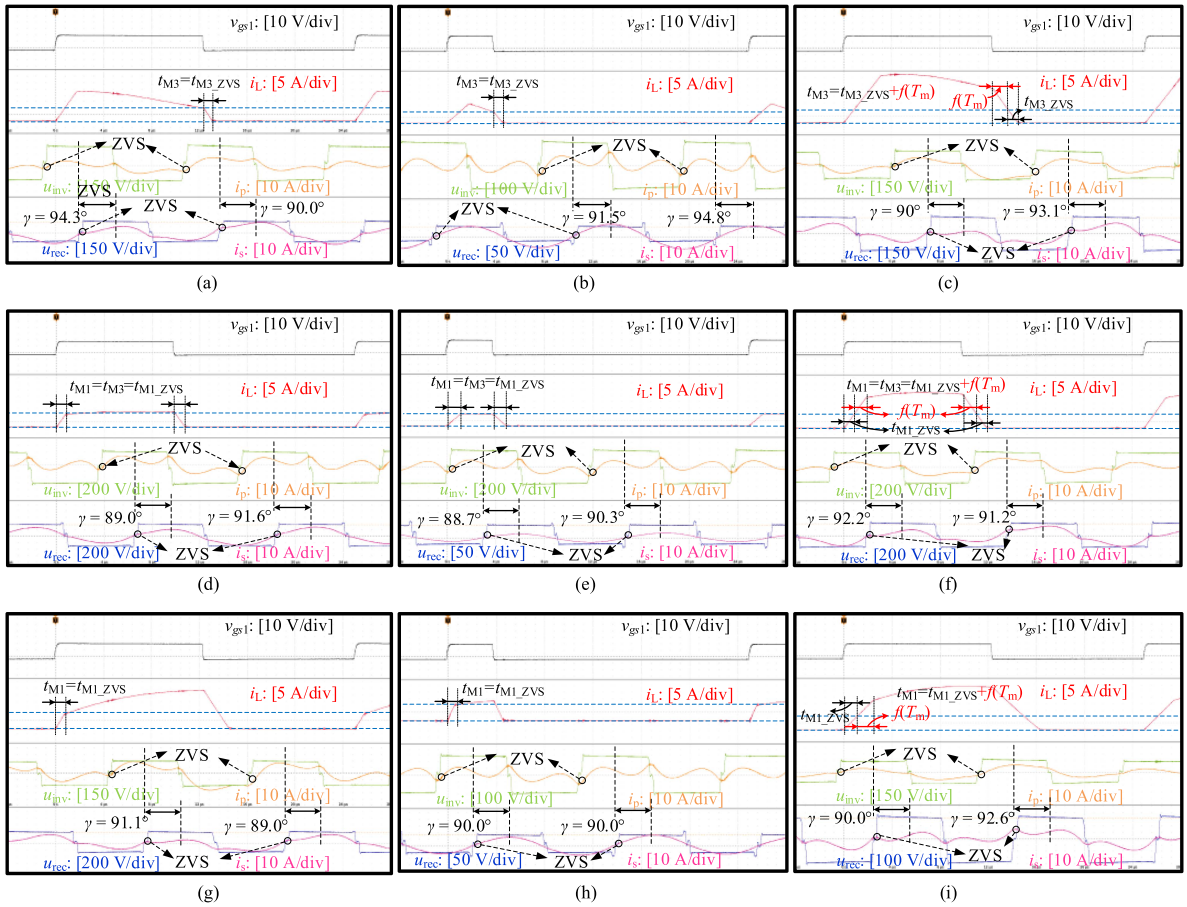

Fig. 26. Proposed modulation scheme conducted in the new time scale T_{m}. (a) Buck mode, $P_{\mathrm{o}} = 1.44$ kW. (b) Buck mode, $P_{\mathrm{o}} = 0.20$ kW. (c) Buck mode, $P_{\mathrm{o}} = 2.25$ kW. (d) Equal mode, $P_{\mathrm{o}} = 1.0$ kW. (e) Equal mode, $P_{\mathrm{o}} = 0.15$ kW. (f) Equal mode, $P_{\mathrm{o}} = 2.06$ kW. (g) Boost mode, $P_{\mathrm{o}} = 1.6$ kW. (h) Boost mode, $P_{\mathrm{o}} = 0.20$ kW. (i) Boost mode, $P_{\mathrm{o}} = 2.36$ kW. (a) Time: 4 μs/div. (b) Time: 4 μs/div. (c) Time: 4 μs/div. (d) Time: 4 μs/div. (e) Time: 4 μs/div. (f) Time: 4 μs/div. (g) Time: 4 μs/div. (h) Time: 4 μs/div. (i) Time: 4 μs/div.

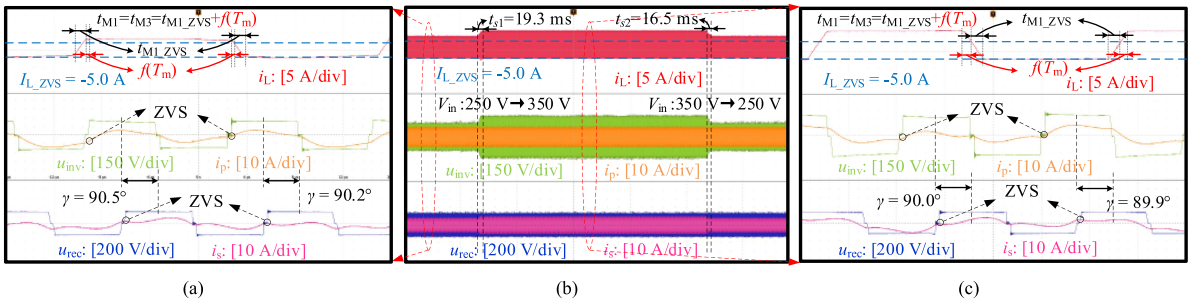

Fig. 27. Proposed modulation scheme conducted at input voltage transients when $\sigma = 1$ and $V_{\mathrm{bat}} = 300$ V. (a) Zoom-in waveforms when $V_{\mathrm{in}} = 250$ V, $P_{\mathrm{o}} = 1.17$ kW. (b) Dynamic operation waveforms. (c) Zoom-in waveforms when $V_{\mathrm{in}} = 350$ V, $P_{\mathrm{o}} = 1.66$ kW. (a) Time: 4 μs/div. (b) Time: 200 ms/div. (c) Time: 4 μs/div.

Based on the analysis in Section IV-E, when $V_{\mathrm{in}} = 250$ V, $V_{\mathrm{bat}} = 350$ V and $V_{\mathrm{in}} = 350$ V, $V_{\mathrm{bat}} = 250$ V, the system output powers are theoretically equal to each other. However, the experimental results show discrepancies of 0.01 kW and 0.02 kW, respectively, and the causes of these discrepancies are consistent with those that lead to the errors in the inductor current $I_{\mathrm{L\_RMS}}$ shown in Figs. 17 and 18.

D. Power Losses and Efficiency Analysis

When $V_{\mathrm{in}} = 320$ V, the curves of dc–dc efficiency of the cascaded system in different operating modes are presented in Fig. 29. It can be observed from Fig. 29 that when the voltage ratio of the first stage σ is 1 and the load voltage is 350 V, the dc–dc efficiency of the cascaded system reaches its peak

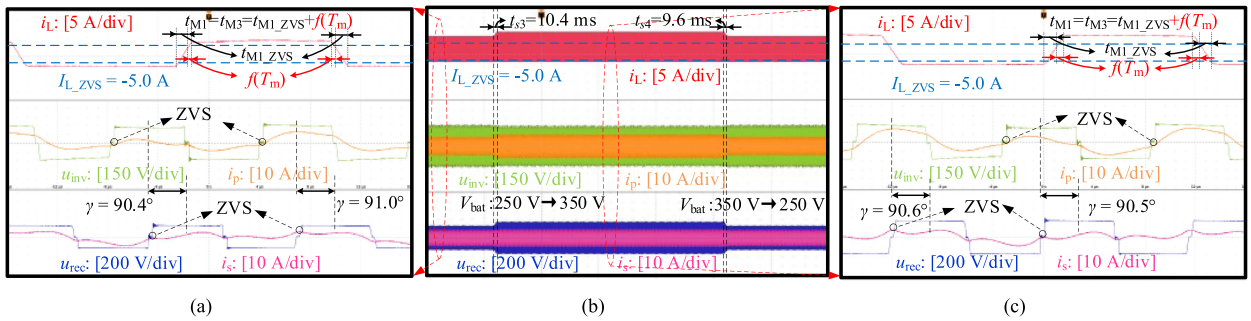

Fig. 28. Proposed modulation scheme conducted at load transients when $\sigma = 1$ and $V_{in} = 300$ V. (a) Zoom-in waveforms when $V_{bat} = 250$ V, $P_o = 1.18$ kW. (b) Dynamic operation waveforms. (c) Zoom-in waveforms when $V_{bat} = 350$ V, $P_o = 1.64$ kW. (a) Time: 4 μs/div. (b) Time: 200 ms/div. (c) Time: 4 μs/div.

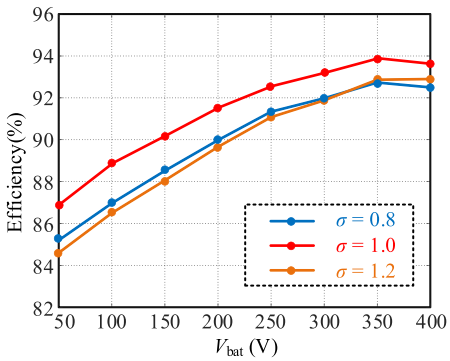

Fig. 29. Measured efficiency with the proposed modulation scheme at different σ when $V_{in} = 320$ V.

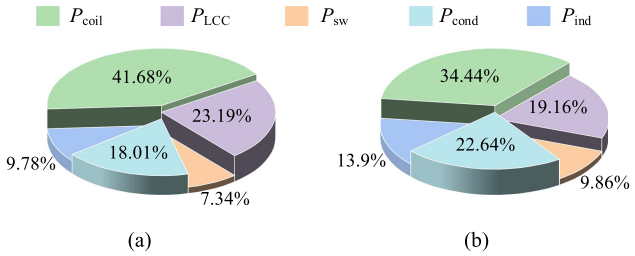

Fig. 30. Loss distribution of the FSBB-IPT system at $\sigma = 1$ when $V_{in} = 320$ V, $V_{bat} = 350$ V. (a) With the proposed scheme. (b) Without the proposed scheme. (a) Total loss: 102.2 W. (b) Total loss: 103.7 W.

at 93.85%. In addition, in the full-power operating ranges of the three modes, the equal mode consistently exhibits higher efficiency compared to the other two modes. The primary reason is that in this mode, t_{M1} is always equal to t_{M3}, and during t_{M2}, the inductor current i_L remains constant, thereby reducing current peaks and achieving minimal loss operation.

In Fig. 30, the calculated loss distributions before and after using the proposed hybrid ZVS modulation scheme of the FSBB-IPT system are presented, where $\sigma = 1$, $V_{in} = 320$ V, $V_{bat} = 350$ V, and $P_o = 1.8$ kW. Here, the switching loss P_{sw} (including switches S_1–S_4, Q_{11}–Q_{14}, and Q_{21}–Q_{24}), the loss in the inductor P_{ind} (including core loss and copper loss), the conduction loss of the switches P_{cond}, the loss in the *LCC–LCC* compensation network P_{LCC}, and the loss of the coupling coils P_{coil} are analyzed. The power losses are obtained based on the calculation methods in [10] and [30]. It can be seen from Fig. 30 that P_{coil} and P_{LCC} account for the majority of the total loss when the cascaded system operates at the peak efficiency. As long as the input and load voltages of the second-stage IPT system remain unchanged, P_{coil} and P_{LCC} will not be affected by the modulation strategy, despite the variation in their proportion of the total loss. As P_{cond} and P_{ind} are proportional to $I^2_{L\_RMS}$, the proportion of their power loss reduces from 22.64% to 18.01% and from 13.9% to 9.78%, with the corresponding decrease values being approximately 9.6 W and 7.2 W, respectively. Moreover, the inductor current of the FSBB converter is limited to $|I_{L\_zvs}|$, which reduces the switching loss P_{sw}. Thus, the proposed hybrid modulation primarily reduces the system's switching loss P_{sw}, and minimizes P_{cond} and P_{ind} by reducing RMS value I_{L_RMS} of the inductor current of the front-end FSBB converter.

E. Comparison and Discussion

Table XI provides a comparison of the proposed modulation method with the existing schemes. As illustrated in Table XI, the advantages of the proposed modulation scheme in this article are as follows.

1) Comparing with the schemes in [11], [12], and [26], the proposed one in this article, only with a 2-D LUT, i.e., the input voltage V_{in} and the output power P_o, the RMS value of the inductor current can be effectively minimized. As a result, this substantially reduces the DSP's memory space to store the LUT and enhances instruction execution speed and operational efficiency.
2) The proposed method is implemented under a new time scale T_m, which effectively reduces the computational burden of DSP compared with the scheme in [10]. The phase shift β enables synchronous modulation of cascaded systems with multiple operating frequencies without communication between the cascaded stages. Therefore, it can be applied in a wider range of scenarios. In addition, maintaining a constant sampling frequency is also more conducive to EMI filter design, effectively reducing interference in PCB circuits.

TABLE XI
COMPARISON WITH EXISTING MODULATION SCHEMES

Literature	[10]	[11]	[12]	[25]	[26]	**This article**
Application scenarios	FSBB	FSBB	FSBB	IPT-FSBB	FSBB	FSBB-IPT
Operating frequency	Multiple	Single	Single	Multiple	Multiple	Two
Dimension of LUT	2D	/	3D	3D	/	2D
Storage space occupation	★★★	/	★★★★	★★★	★★	★★
Sampling frequency	Variable	Constant	Constant	Variable	Variable	Constant
Minimization of $I_{\text{L\_RMS}}$	Yes	No	Yes	Yes	Yes	Yes
Time consumption	Moderate	Long	Long	Long	Short	Short
Complexity	Medium	High	High	High	Medium	Low

3) In three operating modes, reducing the RMS value of the inductor current in the full-power range is achieved with just one modulation variable combined with the LUT, which greatly reduces the complexity of the modulation method.

In this article, the *LCC-LCC* compensated IPT system with the active rectifier on the secondary side, which features high-order characteristic, is chosen as the second stage to illustrate the advantages of the proposed hybrid modulation scheme. If a passive rectifier is used on the secondary side, the losses of the cascaded system will increase, and the modulation degrees of freedom will be reduced. In this case, only the single-PSC strategy can be used and the synchronous modulation of the second-stage IPT system will become ineffective.

VI. CONCLUSION

To increase the model accuracy in a cascaded system with multiple time scales, this article proposes a TTSM for the FSBB-IPT system, which achieves a high accuracy of over 98%. Furthermore, a hybrid ZVS modulation strategy is proposed in the new time scale T_{m}, significantly reducing execution time. In addition, it leverages inherent phase shift for synchronous modulation. Experimental results demonstrate that this strategy can achieve up to 93.85% peak efficiency.

APPENDIX

The matrices $\boldsymbol{M}_i$ and $\boldsymbol{N}_i$ mentioned in Section III are given as follows:

$$\boldsymbol{M}_i = [\boldsymbol{M}_{11}\boldsymbol{M}_{12}; \boldsymbol{M}_{21}\boldsymbol{M}_{22}; \boldsymbol{M}_{31}\boldsymbol{M}_{32}; \boldsymbol{M}_{41}\boldsymbol{M}_{42}]$$

$$\boldsymbol{M}_{11(\text{A})} = \begin{pmatrix} 0 & -1/L & 0 \\ 1/C_{\text{f}} & 0 & -1/C_{\text{f}} \end{pmatrix}$$

$$\boldsymbol{M}_{11(\text{B})} = \begin{pmatrix} 0 & -1/L & 0 \\ 1/C_{\text{f}} & 0 & 0 \end{pmatrix}$$

$$\boldsymbol{M}_{12} = \boldsymbol{0}_{2\times 7}$$

$$\boldsymbol{M}_{21} = \begin{pmatrix} 0 & 1/L_{\text{p}} & 0 \end{pmatrix}, \boldsymbol{M}_{22} = \begin{pmatrix} -1/L_{\text{p}} & 0 & 0 & 0 & 0 & 0 & 0 \end{pmatrix}$$

$$\boldsymbol{M}_{31} = \begin{pmatrix} 0 & 0 & 1/C_{\text{p}} \end{pmatrix}, \boldsymbol{M}_{32} = \begin{pmatrix} 0 & 0 & -1/C_{\text{p}} & 0 & 0 & 0 & 0 \end{pmatrix}$$

$$\boldsymbol{M}_{41} = \boldsymbol{0}_{7\times 3}$$

$$\boldsymbol{M}_{42} = \begin{pmatrix} 0 & 0 & 1/C_1 & 0 & 0 & 0 & 0 \\ L_2/\Delta & -L_2/\Delta & 0 & 0 & -M/\Delta & -M/\Delta & 0 \\ -M/\Delta & M/\Delta & 0 & 0 & L_1/\Delta & L_1/\Delta & 0 \\ 0 & 0 & 0 & 0 & -1/C_2 & 0 & 0 \\ 0 & 0 & 0 & -1/C_{\text{s}} & 0 & 0 & 1/C_{\text{s}} \\ 0 & 0 & 0 & 0 & 0 & 1/L_{\text{s}} & 0 \end{pmatrix}$$

$$\boldsymbol{N}_1 = \begin{bmatrix} 1/L & 0 & 0 & 0 & 0 & 0 & 0 & 0 & 0 & 0 \end{bmatrix}^T$$

$$\boldsymbol{N}_2 = \begin{bmatrix} 0 & 0 & 0 & 0 & 0 & 0 & 0 & 0 & 0 & 1/L_{\text{s}} \end{bmatrix}^T$$

$$I_{L\_\text{RMS}}^2 = I_{L0}^2 + f_{\text{M}}[V_{\text{in}}^2(t_{\text{M1}} + t_{\text{M2}})^3 - V_{\text{in}}(t_{\text{M1}} + t_{\text{M2}})^2 (-3I_{L0}L - \sigma V_{\text{in}} t_{\text{M1}} + 2\sigma V_{\text{in}} t_{\text{M2}}) - \sigma V_{\text{in}} \left(-3I_{L0}Lt_{\text{M1}}^2 + 3I_{L0}Lt_{\text{M2}}^2 - \sigma V_{\text{in}} t_{\text{M2}}^3\right)]/\left(3\sigma L^2\right).$$

REFERENCES

[1] Z.-P. Yuan, P. Li, Z.-L. Li, and J. Xia, "Data-driven risk-adjusted robust energy management for microgrids integrating demand response aggregator and renewable energies," *IEEE Trans. Smart Grid*, vol. 14, no. 1, pp. 365–377, Jan. 2023.

[2] F. Liu, C. Chen, C. Lin, G. Li, H. Xie, and Z. Bie, "Utilizing aggregated distributed renewable energy sources with control coordination for resilient distribution system restoration," *IEEE Trans. Sustain. Energy*, vol. 14, no. 2, pp. 1043–1056, Apr. 2023.

[3] K. He, X. Liu, F. Gao, X. Yang, Z. Cheng, and D. Liu, "Accurate discrete-time modeling and boundary analysis for high-order wireless power transfer systems," *IEEE Trans. Power Electron.*, vol. 39, no. 12, pp. 16839–16854, Dec. 2024.

[4] Z. Yan, K. Zhang, L. Qiao, Y. Hu, and B. Song, "A multiload wireless power transfer system with concentrated magnetic field for AUV cluster system," *IEEE Trans. Ind. Appl.*, vol. 58, no. 1, pp. 1307–1314, Jan./Feb. 2022.

[5] Z. Yan et al., "Free-rotation wireless power transfer system based on composite anti-misalignment method for AUVs," *IEEE Trans. Power Electron.*, vol. 38, no. 4, pp. 4262–4266, Apr. 2023.

[6] S. Roy, A. N. M. W. Azad, S. Baidya, M. K. Alam, and F. Khan, "Powering solutions for biomedical sensors and implants inside the human body: A comprehensive review on energy harvesting units, energy storage, and wireless power transfer techniques," *IEEE Trans. Power Electron.*, vol. 37, no. 10, pp. 12237–12263, Oct. 2022.

[7] N. U. Hassan, S.-W. Hong, and B. Lee, "A robust multioutput self-regulated rectifier for wirelessly powered biomedical applications," *IEEE Trans. Ind. Electron.*, vol. 68, no. 6, pp. 5466–5472, Jun. 2021.

[8] S. Wu, C. Cai, X. Liu, W. Chai, and S. Yang, "Compact and free-positioning omnidirectional wireless power transfer system for unmanned aerial vehicle charging applications," *IEEE Trans. Power Electron.*, vol. 37, no. 8, pp. 8790–8794, Aug. 2022.

[9] Y. Zhang, S. Chen, X. Li, and Y. Tang, "Design methodology of free-positioning nonoverlapping wireless charging for consumer electronics based on antiparallel windings," *IEEE Trans. Ind. Electron.*, vol. 69, no. 1, pp. 825–834, Jan. 2022.
[10] F. Liu, J. Xu, Z. Chen, P. Yang, K. Deng, and X. Chen, "A multi-frequency PCCM ZVS modulation scheme for optimizing overall efficiency of four-switch buck–boost converter with wide input and output voltage ranges," *IEEE Trans. Ind. Electron.*, vol. 70, no. 12, pp. 12431–12441, Dec. 2023.
[11] H. J. Ahmad and M. Hagiwara, "A compact high-power noninverting bidirectional buck–boost chopper for onboard battery energy storage systems," *IEEE Trans. Power Electron.*, vol. 37, no. 2, pp. 1722–1735, Feb. 2022.
[12] J. Liao, G. Qiu, Y. Huang, and V. Khadkikar, "Lagrange-multiplier-based control method to optimize efficiency for four-switch buck–boost converter over whole operating range," *IEEE Trans. Ind. Electron.*, vol. 71, no. 1, pp. 822–833, Jan. 2024.
[13] X. Zhang, T. Wang, H. Bao, Y. Hu, and B. Bao, "Stability effect of load converter on source converter in a cascaded buck converter," *IEEE Trans. Power Electron.*, vol. 38, no. 1, pp. 604–618, Jan. 2023.
[14] H. Ji, F. Xie, Y. Chen, and B. Zhang, "Small-step discretization method for modeling and stability analysis of cascaded DC–DC converters with considering different switching frequencies," *IEEE Trans. Power Electron.*, vol. 37, no. 8, pp. 8855–8872, Aug. 2022.
[15] C. Cheng, F. Xie, B. Zhang, D. Qiu, W. Xiao, and H. Ji, "Modeling and nonlinear dynamic analysis of cascaded DC–DC converter systems based on simplified discrete mapping," *IEEE Trans. Ind. Electron.*, vol. 70, no. 6, pp. 5830–5839, Jun. 2023.
[16] B. He, W. Chen, H. Mu, D. Zhan, and C. Zhang, "Small-signal stability analysis and criterion of triple-stage cascaded DC system," *IEEE J. Emerg. Sel. Topics Ind. Electron.*, vol. 10, no. 2, pp. 2576–2586, Apr. 2022.
[17] Q.-C. Zhong and X. Zhang, "Impedance-sum stability criterion for power electronic systems with two converters/sources," *IEEE Access*, vol. 7, pp. 21254–21265, 2019.
[18] X. Zhang, Q.-C. Zhong, and W.-L. Ming, "Stabilization of cascaded DC/DC converters via adaptive series-virtual-impedance control of the load converter," *IEEE Trans. Power Electron.*, vol. 31, no. 9, pp. 6057–6063, Sep. 2016.
[19] A. Aldhaheri and A. H. Etemadi, "Stabilization and performance preservation of DC–DC cascaded systems by diminishing output impedance magnitude," *IEEE Trans. Ind. Appl.*, vol. 54, no. 2, pp. 1481–1489, Mar./Apr. 2018.
[20] J. Liao, C. Guo, Y. Huang, G. Qiu, N. Zhou, and Q. Wang, "Active damping control of cascaded DC converter in DC microgrids based on optimized parallel virtual resistance," *IEEE J. Emerg. Sel. Topics Ind. Electron.*, vol. 4, no. 2, pp. 560–570, Apr. 2023.
[21] Y. Li, Q. Li, B. Ji, and S. Duan, "A ZVS control scheme for high-efficiency buck–boost current-fed isolated DC–DC converter," *IEEE Trans. Transport. Electrific.*, vol. 9, no. 3, pp. 4223–4235, Sep. 2023.
[22] S. Zhu, W. Han, J. Chen, and Q. Liu, "Closed-form solution for ZVS and minimum current of cascaded buck + boost converters eliminating instantaneous inductor current detection," *IEEE Trans. Power Electron.*, vol. 38, no. 10, pp. 12455–12468, Oct. 2023.
[23] X. Qi, Y. Wang, Y. Wang, and Z. Chen, "Optimization of centralized equalization systems based on an integrated cascade bidirectional DC–DC converter," *IEEE Trans. Ind. Electron.*, vol. 69, no. 1, pp. 249–259, Jan. 2022.
[24] J. Fang, X. Ruan, X. Huang, R. Dong, X. Wu, and J. Lan, "A PWM plus phase-shift control for four-switch buck-boost converter to achieve ZVS in full input voltage and load range," *IEEE Trans. Ind. Electron.*, vol. 69, no. 12, pp. 12698–12709, Dec. 2022.
[25] G. Yu, J. Dong, T. B. Soeiro, G. Zhu, Y. Yao, and P. Bauer, "Three-mode variable-frequency ZVS modulation for four-switch buck+boost converters with ultra-high efficiency," *IEEE Trans. Power Electron.*, vol. 38, no. 4, pp. 4805–4819, Apr. 2023.
[26] L. Tian, X. Wu, C. Jiang, and J. Yang, "A simplified real-time digital control scheme for ZVS four-switch buck–boost with low inductor current," *IEEE Trans. Ind. Electron.*, vol. 69, no. 8, pp. 7920–7929, Aug. 2022.
[27] J. Schonberger, "A single phase multi-string PV inverter with minimal bus capacitance," in *Proc. 13th Eur. Conf. Power Electron. Appl.*, Sep. 2009, pp. 1–10.
[28] H. Hu, S. Harb, N. Kutkut, I. Batarseh, and Z. J. Shen, "A review of power decoupling techniques for microinverters with three different decoupling capacitor locations in PV systems," *IEEE Trans. Power Electron.*, vol. 28, no. 6, pp. 2711–2726, Jun. 2013.
[29] A. Namadmalan, J. M. Alonso, and A. Iqbal, "Accurate fundamental harmonic modeling of inductive power transfer battery chargers," *IEEE Trans. Transport. Electrif.*, vol. 8, no. 1, pp. 627–635, Mar. 2022.
[30] Y. Jiang, L. Wang, J. Fang, R. Li, R. Han, and Y. Wang, "A high-efficiency ZVS wireless power transfer system for electric vehicle charging with variable angle phase shift control," *IEEE J. Emerg. Sel. Topics Power Electron.*, vol. 9, no. 2, pp. 2356–2372, Apr. 2021.
[31] X. Zhang et al., "A control strategy for efficiency optimization and wide ZVS operation range in bidirectional inductive power transfer system," *IEEE Trans. Ind. Electron.*, vol. 66, no. 8, pp. 5958–5969, Aug. 2019.

Kai He (Student Member, IEEE) received the B.S. degree in electrical engineering from the East China University of Science and Technology, Shanghai, China, in 2021. He is currently working toward the Ph.D. degree in electrical engineering with Shanghai Jiao Tong University, Shanghai, China.

His research interests include multiple-time-scale modeling and control of cascaded systems and ZVS modulation of dc–dc converters.

Fei Gao (Member, IEEE) received his Ph.D. degree in electrical engineering from the Power Electronics, Machines, and Control Research Group, University of Nottingham, Nottingham, U.K., in 2016.

From 2010 to 2012, he was with Jiangsu Electric Power Research Institute, Nanjing, State Grid Corporation of China. From 2016 to 2019, he was with the Department of Engineering Science, University of Oxford, U.K., as a Postdoctoral Researcher. Since July 2019, he has been with Shanghai Jiao Tong University, Shanghai, China, as an Associate Professor. His current research interests include microgrids, more electric transportation systems, and wireless power transfer.

Dr. Gao was a recipient of the European Union Clean Sky Best Ph.D. Award in 2017 and IET Control and Automation Runner-Up Ph.D. Award in 2018.

Xin Liu (Member, IEEE) received the B.S. degree in electrical engineering from Wuhan University, Wuhan, China, in 2015, and the Ph.D. degree in electrical engineering from Shanghai Jiao Tong University, Shanghai, China, in 2019.

From 2019 to 2021, he was with Huawei Technologies, Company, Ltd. From 2021 to 2023, he was with the Department of Electrical Engineering, Shanghai Jiao Tong University, Shanghai, China, as a postdoctoral researcher. Since September 2023, he has been with the Shenzhen Institute for Advanced Study, University of Electronic Science and Technology of China, Chengdu, China, as an Associate Researcher. His current research interests include wireless power transfer and solid-state transformers.

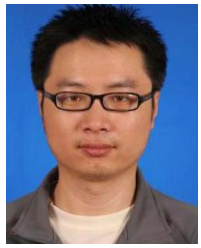

Ying Jiang received the Ph.D. degree in electrical engineering from Shanghai Jiao Tong University, Shanghai, China, in 2011.

Since 2011, he has been working with Shanghai Dianji University, Shanghai, China, where he has been an Associate Professor. His current research interests include power electronics magnetic integration, wireless power transfer, and more electric transportation systems.

Xijun Yang (Member, IEEE) received the Ph.D. degree in control engineering from Shanghai University, Shanghai, China, in 2002.

From 1992 to 1995, he was an electrical engineer with the Handan Institute of Coal Mine Design and Research, Hebei, China. From 2013 to 2014, he was a Guest Associate Professor with the Department of Energy Technology, Aalborg University, Denmark. From 2004 to 2013 and from 2014 till now, he has worked with the Department of Electrical Engineering, Shanghai Jiao Tong University as an Associate Professor. His current research interests include wireless power transfer, power conversion, and solid-state transformers.

Daniel J. Rogers (Senior Member, IEEE) received the M.Eng. and Ph.D. degrees in electrical and electronic engineering from Imperial College London, London, U.K., in 2007 and 2011, respectively.

He is currently an Associate Professor with the Department of Engineering Science, University of Oxford, Oxford, U.K. He conducts research in collaboration with industry and has been an investigator on U.K. EPSRC research projects in the areas of power electronics, grid-scale energy storage, and microgrids. His research interests include power electronics ranging from active control of transistor switching to circuit and control system design, through to novel applications enabled by wide-bandgap devices.